



Universidad Autónoma
de Madrid

Biblos-e Archivo
Repositorio Institucional UAM

Repositorio Institucional de la Universidad Autónoma de Madrid

<https://repositorio.uam.es>

Esta es la **versión de autor** del artículo publicado en:

This is an **author produced version** of a paper published in:

Applied Catalysis B: Environmental 253 (2019): 253-262

DOI: <https://doi.org/10.1016/j.apcatb.2019.04.040>

Copyright: © 2019 Elsevier B.V. This manuscript version is made available under the CC-BY-NC-ND 4.0 licence <http://creativecommons.org/licenses/by-nc-nd/4.0/>

El acceso a la versión del editor puede requerir la suscripción del recurso

Access to the published version may require subscription

Mixed Ti-Zr metal-organic-frameworks for the photodegradation of acetaminophen under solar irradiation

A. Gómez-Avilés¹, M. Peñas-Garzón¹, J. Bedia^{1,*}, D.D. Dionysiou²,
J.J. Rodríguez¹, C. Beller¹

¹ *Departamento de Ingeniería Química, Universidad Autónoma de Madrid, Campus Cantoblanco, E-28049 Madrid, Spain*

² *Environmental Engineering and Science Program, Department of Chemical and Environmental Engineering (ChEE), 705 Engineering Research Center, University of Cincinnati, Cincinnati, OH 45221-0012, USA*

*Corresponding author. E-mail address: jorge.bedia@uam.es

Abstract

Mixed Ti-Zr metal-organic-frameworks (MOFs) have been synthesized and tested as photocatalysts under solar-simulated radiation using acetaminophen (ACE) as target pollutant. These materials were obtained upon partial substitution of Ti by Zr atoms in the crystalline structure of NH₂-MIL-125(Ti) MOF. The effect of the Ti:Zr molar ratio on their characteristics and catalytic behaviour has been analysed. Materials with high Zr relative amount (60-80%) showed amorphous structure and low solar-photocatalytic activity. In contrast, lower Zr proportions resulted in new MOFs with well-defined crystalline structure and high activity for the solar photocatalytic degradation of ACE, even higher than that of the bare Ti MOF. Results with scavengers allowed concluding that O₂^{•-} radicals are the main reactive species, although photogenerated [•]OH radicals and electrons also contribute to the degradation. The stability of the most active photocatalyst was confirmed upon three successive runs.

Keywords: Metal organic framework; NH₂-MIL-125; solar photocatalysis; water purification; acetaminophen.

1. Introduction

Metal-organic frameworks (MOFs) are hybrid materials composed of metal ions connected by organic linkers. These crystalline networks present structures with well-defined porosity, large specific surface area and the possibility of modulating their physicochemical properties by selecting different organic building blocks or metal clusters [1,3]. MOFs have attracted major attention in a wide range of applications, including gas storage [4,6], photoelectronic sensors [7,8], membrane processes [9,10] and environmental remediation [11]. Furthermore, these materials are gaining relevance as catalysts, including photocatalysts due to their semiconductor characteristics [12]. When a semiconductor solid is irradiated with an energy equal to or higher than its band gap, electrons (e^-) are promoted from the valence band (VB, formed by orbitals of the organic linker in the case of MOFs) to the conduction band (CB, associated to orbitals of the metal cluster in MOFs), generating holes (h^+) in the VB [1]. These photogenerated charges can be directed towards the surface of the material and be involved in the formation of powerful oxidizing species, which can degrade pollutant molecules. The earliest works dealing with MOFs used in photocatalytic water treatment date back to the beginning of the 2000's, when Yu et al. [13] proved the photocatalytic activity of these materials for the degradation of methylene blue dye. Later, Mahata et al. [14] explored the breakdown of selected organic dyes with three different coordination polymers. Since then, different modifications of MOFs, affecting both the organic linkers and/or the metal centres, have been researched to enhance their photocatalytic activity [15-17].

Regarding photocatalytic applications, many studies have used Ti-containing MOFs. One of the most widely analysed is $[Ti_8O_8(OH)_4(C_8H_6O_4)_6]$, denoted as MIL-125(Ti), which was synthesized for the first time by Dan-Hardi et al. [18] in 2009. MIL-125(Ti) presents a band gap energy of 3.6 eV (corresponding to a wavelength $\lambda = 345$ nm), being photoactive only under UV-light. Many efforts have been made to increase its photochemical activity towards the solar light, in order to avoid the use of UV-lamps and reduce the treatment cost. The incorporation of a $-NH_2$ group to the organic linker gives rise to NH_2 -MIL-125(Ti) MOF, $[Ti_8O_8(OH)_4(C_8H_5O_4NH_2)_6]$, allowing the donation of N_{2p} electrons of the aromatic structure to the amine group. This behaviour results in the formation of a redshifted band at the VB of the MOF, displacing the absorption band towards the visible region and reducing the band gap value (2.7 eV, $\lambda = 460$ nm) [19,20]. In addition to this, the amine group enhances the

charge transfer between metal and organic linker, the long-lived photoexcited states, inhibiting electron-hole recombination [1,2,21,22]. Zr-based MOFs have been also extensively studied in photocatalytic applications, being UiO-66 a well-known example of this kind of materials [23]. The presence of Zr^{4+} , a high oxidation state metal, gives rise to a strong coordination bonds with the organic linker [24,25]. Furthermore, it has been previously reported that Zr doping increases the solar photocatalytic activity of TiO_2 [26].

Emerging pollutants, including pharmaceuticals, personal care products, pesticides and hormones, are currently found in wastewaters and are considered potentially hazardous due to their harmful impact over the endocrine system and the environment [27,28]. Their removal from water streams is the focus of intense research and applications by the scientific community. The novelty of this study is the synthesis of new mixed Ti-Zr MOFs with different Ti:Zr molar ratios based on $\text{NH}_2\text{-MIL-125(Ti)}$. To the best of our knowledge, this is the first mixed Zr-Ti MOF apart from the previous reported by Lee et al. [29]. Although in that study, Ti was introduced in the Zr-based MOF in a postsynthetic exchange, while in our study we introduce Zr atoms in a Ti-based MOF in a single step, avoiding the use of postsynthetic steps. The solar photocatalytic activity of this material has been tested in the degradation of acetaminophen, as target emerging pollutant, in aqueous phase. This compound is a widely used antipyretic and analgesic pharmaceutical and its presence has been detected in urban wastewaters. Despite, $\text{NH}_2\text{-MIL-125(Ti)}$ has been recently used as photocatalyst for the reduction of heavy metals [30], the oxidation of alcohols and amines [31-33] and the degradation of dyes [19,20,34] under UV and visible light, to the best of our knowledge no previous works have reported on the synthesis of mixed Ti-Zr MOFs based on $\text{NH}_2\text{-MIL-125}$ and their application for the degradation of emerging pollutants.

2. Experimental

2.1. Materials synthesis

Pure $\text{NH}_2\text{-MIL-125(Ti)}$ was synthesized according to Martis et al. [35] with some modifications. 2-amino benzene dicarboxylic acid (6 mmol, Aldrich, 99%) was mixed with N,N-dimethylformamide (25 mL, DMF, Sigma-Aldrich, $\geq 99.8\%$) and stirred at room temperature for 5 min until total dissolution. Then, titanium isopropoxide (3 mmol, Aldrich, $\geq 97\%$) was added dropwise under continuous stirring until complete homogenization and afterwards methanol (25 mL, CH_3OH , Sigma-Aldrich, anhydrous 99.8%) was incorporated.

The mixture was stirred for 30 min, transferred to a 65 mL Teflon lined stainless steel autoclave, and heated for 16 h at 150 °C. After the solvothermal treatment, the resulting solid was separated by centrifugation (5000 rpm, 5 min). Further, it was washed twice with 100 mL of DMF for 30 min and twice with 100 mL of methanol during the same time, separating the resulting solid by centrifugation in all cases. The final yellow solid was dried at 60 °C overnight. This MOF was denoted as Ti. The mixed Ti-Zr MOFs were synthesized following the same procedure but with different Ti:Zr molar percentages combining zirconium (IV) butoxide solution (Aldrich, 80%wt in butanol) and titanium isopropoxide in the metal-precursor incorporation step of the synthesis. The mixed Ti-Zr MOFs were denoted according to the zirconium molar percentage incorporated, which was determined by wavelength-dispersive X-ray fluorescence (WDXRF). Four mixed-MOFs were prepared, denoted by TiZr15, TiZr30, TiZr60 and TiZr80.

2.2. Characterization

A Bruker D8 diffractometer with a Sol-X energy dispersive detector was used to record the X-ray diffraction (XRD) spectra from 2 to 50° of 2θ , using a Cu K α radiation and a recording rate equal to 1.5 °·min⁻¹. The (121) diffraction peak was used to calculate the average crystal size of the MOF and the UnitCell software [36] was used to estimate the cell parameters of the MOF unit crystal by a minimum square approximation. A TriStar 123 equipment (Micromeritics) was used to characterize the porous texture by N₂ adsorption-desorption at -196 °C. Prior to the analyses, the samples were outgassed under vacuum at 120 °C for 18 h. The BET method was used to calculate the specific surface area (S_{BET}). The micropore surface area (S_{MP}) and the external or non-microporous surface area (S_{EXT}) were obtained from the t-plot. The total pore volume (V_{T}) was assessed by the amount of nitrogen adsorbed (as liquid) at P/P_0 of 0.99. The density functional theory (DFT) was used to obtain the pore size distribution [37]. A Shimadzu 2501PC UV-vis spectrophotometer was employed for recording the UV-vis diffuse reflectance spectra (DRS) in the 250-800 nm range (BaSO₄ was chosen as reference). The spectra were used to obtain the band gap values of the photocatalysts, considering them as indirect semiconductors [38] (as TiO₂), using the Tauc Plot technique [39]. The amount of Ti and Zr in the different photocatalysts was determined by wavelength-dispersive X-ray fluorescence (WDXRF) using a Bruker S8 TIGER spectrometer under inert atmosphere (He) with a 4 kW Rh-anode X-ray tube (maximum voltage of 60 kV and maximum current of 170 mA). The composition was determined by

using Spectra Plus (v.3) software. Scanning electron microscopy (SEM) images were obtained with a Quanta 3D FEG apparatus from FEI COMPANY. A Bruker iFS 66VS spectrometer was used to record the Fourier Transform Infrared (FTIR) spectra, using a resolution of 2 cm^{-1} in the $4000\text{--}400\text{ cm}^{-1}$ wavenumber range. Raman spectra were obtained using a 532 nm laser μ Sense-LabC1X Enwave Optronics Raman Confocal equipment, coupled to an Olympus BX51 M microscope. Photoluminescence (PL) spectra of the materials were obtained via a Fluoromax-4 spectrofluorometer with an excitation wavelength of 420 nm.

2.3 Photocatalytic tests

The photocatalytic degradation of acetaminophen (ACE) (Sigma-Aldrich, >99%) was carried out in a Pyrex jacketed reactor (500 mL) at a controlled temperature of $20\text{ }^{\circ}\text{C}$ under magnetic stirring. This reactor was placed inside the chamber of a solar simulator (Suntest XLS+, ATLAS) with a Xe lamp and a “Daylight” filter (cuts off $\lambda \leq 290\text{ nm}$), capable of simulating solar radiation. The light intensity was set at $600\text{ W}\cdot\text{m}^{-2}$. In each test, a catalyst amount of $250\text{ mg}\cdot\text{L}^{-1}$ was dispersed in 150 mL aqueous solution containing an initial concentration of ACE of $5\text{ mg}\cdot\text{L}^{-1}$ at an initial pH equal to 6.9 (unless different conditions were indicated). The reactor was covered and the dispersion was maintained under stirring in dark for 1 h with the aim of achieving adsorption equilibrium. Afterwards, the solution was exposed to simulated solar light for 6 h. Samples of 0.45 mL were taken at different times, filtered with PTFE syringeless filters (Whatman $0.2\text{ }\mu\text{m}$) and analysed by HPLC (Shimadzu Prominence-I LC-2030C), using a diode array detector (SPD-M30A) and a C18 column (Eclipse Plus $5\text{ }\mu\text{m}$, Agilent). The chromatograms were registered using a gradient elution method where the mobile phase content (acetic acid aqueous solution 0.1%, Sigma Aldrich $\geq 99\%$) changes during elution with acetonitrile (Scharlau HPLC grade) at a rate of $0.56\%\cdot\text{min}^{-1}$, with a constant flow equal to $0.7\text{ mL}\cdot\text{min}^{-1}$. Blank tests were carried out without catalyst at the same conditions in order to check the stability of ACE under solar irradiation. Total organic carbon (TOC) was measured with a Shimadzu TOC equipment and organic acids from the ACE photodegradation were analysed by ionic chromatography with a Metrohm 883 Basic IC Plus equipment.

3. Results and discussion

3.1. Characterization

As indicated before, the incorporation of Zr^{4+} in the structure of $\text{NH}_2\text{-MIL-125(Ti)}$ MOF was accomplished by combining Ti^{4+} and Zr^{4+} alkoxide precursors in the desired ratio during the synthetic pathway. The chemical compositions of the samples, collected in Table S1 of the supplementary data, were determined by WDXRF analysis in order to quantify the final Ti/Zr molar ratios. These analyses confirm the successful incorporation of Zr^{4+} in the resulting material. Figure 1 represents the XRD spectra of the different Ti-Zr MOFs synthesized. The diffraction pattern of Ti sample (that without Zr) corresponds to that described in the literature for $\text{NH}_2\text{-MIL-125(Ti)}$ MOF [19,40,42]. In the case of the samples with Zr, those with lower amounts (TiZr15 and TiZr30) show diffraction patterns very similar to that of the Ti sample. In contrast, the diffractograms of the samples with higher amount of Zr (TiZr60 and TiZr80) do not show the characteristic peaks of the crystalline structure and only displayed a wide band at 2θ values close to 7° and associated to an amorphous structure. It seems that the incorporation of Zr in high proportion inhibits the crystallization of the MOF. It is also noteworthy that no other crystalline phases were found in the diffractograms.

Figure 1. XRD patterns. The characteristic peaks of the MIL-125 (ref. ja903726m_si_002.cif [18]) are included as reference (red colour).

The comparison between the diffraction patterns of Ti, TiZr15 and TiZr30 shows a slight negative shift of the most intense peak located at 6.79° of 2θ for Ti sample. This deviation could be attributed to some modification on the crystal lattice of the MOF due to the Zr incorporation. The crystal size and the lattice parameters were analysed in more detail (the data are collected in Table 1). The average crystal size (D) was established by the Scherrer's equation using the (121) peak ($2\theta = 11.6^\circ$). The most intense peak (011) centred at 6.79° was not used because the reference pattern revealed that it overlaps with a lower intensity peak (110) located at 6.69° [18]. The D values show that the incorporation of Zr caused a slight increase of the crystal size and it is interesting to note that TiZr15 and TiZr30 present similar D values, without the Zr percentage having a significant influence. The lattice parameters of the orthorhombic structure characteristics of $\text{NH}_2\text{-MIL-125}$ MOF are also modified by the Zr incorporation. This can be clearly observed in the values of a parameter and cell volume. The orthorhombic structure suffers a high expansion along the x direction accompanied by a certain increase of height (c parameter) and practically no variation in the y axis. These structural modifications are consequence of the substitution of Ti^{4+} in oxo-clusters by bigger

Zr^{4+} atoms [41,43], indicating that the synthetic route used in this work achieves the incorporation of Zr^{4+} into the $\text{NH}_2\text{-MIL-125}$ lattice without the formation of other crystalline phases, giving rise mixed Ti-Zr MOFs.

Table 1. Structural parameters.

Figure 2 shows characteristic SEM images of the synthesized materials. The morphology of Ti was thin and disk-like shapes with an average size of ca. 500 nm, in agreement with the morphology and size previously reported in the literature [34,44,45]. The introduction of Zr seems to have no relevant effect in the morphology of the resulting MOF up to Ti:Zr molar ratios of 70:30. In contrast, further increases in the amount of Zr provoked significant morphological changes. In the case of the TiZr60 sample disc-shaped particles were also obtained, although not so well-defined as those obtained with higher Ti:Zr ratios and with a significantly bigger size (around 1.0-1.5 μm). Finally, the sample with the lowest Ti:Zr ratio (i.e. the highest Zr content, TiZr80) shows a completely amorphous structure. It seems that a high amount of Zr prevents the formation of crystalline structure. Probably other synthesis conditions, namely temperature or duration of the treatment, may lead to the formation of crystals.

Figure 2. SEM images of (A) Ti, (B) TiZr15, (C) TiZr30, (D) TiZr60 and (E) TiZr80.

Figure 3 depicts the N_2 adsorption-desorption isotherms at -196 °C of the synthesized samples. Ti exhibits a type I-like isotherm according to the IUPAC classification with no hysteresis loop, characteristic of a microporous structure and in agreement with previous works [40,46]. Increasing Zr proportion does not modify significantly the shape of the isotherms but clearly reduces the amount of N_2 adsorbed, thus indicating a significant decrease of the microporosity and the BET surface area. The effect is dramatically pronounced at the highest Zr proportions. It may be related to the amorphous character of these materials, without the characteristic channels structure of metal organic frameworks. It seems that the increase in the amount of Zr precursor in the synthesis stage hinders the crystallization, and the lack of a proper crystal lattice results in the loss of porosity. Table 2 summarizes the porous texture parameters of the materials synthesized. It can be seen the

dramatic decrease of BET surface area and micropore volume of the samples with higher Zr proportions. It is noteworthy that low Zr substitution yields a material (TiZr15) with high surface area, similar to that described by the non-Zr NH₂-MIL-125 MOF. The micropore size distributions obtained by DFT (Figure 4) show predominantly narrow microporous structures for the Ti-Zr MOFs with lower Zr proportions, which displace towards higher micropore widths as that proportion increases. These results indicate that while the Zr incorporation induces structural modifications, it does not develop a new porous network and pore tenability.

Figure 3. Nitrogen adsorption–desorption isotherms at -196 °C.

Table 2. Porous texture parameters and band gap values.

Figure 4. DFT pore size distributions.

Figure 5A depicts the UV-Vis absorption spectra of the samples. Ti shows two absorption bands at 280 and 370 nm. The first one is associated to the light absorption of Ti-oxo-clusters, while the second is due to the amine ligand-based absorption [30,41,42]. The introduction of Zr does not significantly affect these values of the absorption bands, except for lowest Ti:Zr molar ratios (TiZr60 and TiZr80). In these cases, the first absorption band shifted to lower wavelengths, ca. 260 nm, which can be attributed to the predominant absorption of Zr-oxo-clusters instead of Ti-oxo-clusters [41]. It is also noteworthy the slight shift in the visible range of absorption of TiZr60. The band gaps (E_g) of these materials were calculated from the Tauc plots (represented in Figure 5B) assuming that they are indirect semiconductors. The values are summarized in Table 2. The estimated band gap for Ti, 2.74 eV, is agreement with the values reported in previous works [19,20]. It corresponds to the electron transfer from the organic linker to the metal-oxo cluster, following the ligand-to-metal charge transfer mechanism [47]. The partial substitution of Ti⁴⁺ by Zr⁴⁺ in the crystal lattice reduces somewhat the band gap at low to moderate Zr content and then increasing the amount of Zr this effect disappears. Therefore, there is a given Ti:Zr ratio associated to a minimum band gap value, although of low significance. Figure S1 represents the light harvesting efficiency (LHE) values obtained from the UV-Vis absorption spectra. As can be seen, all the MOFs

show very similar values apart from TiZr60, which shows slightly higher LHE values in the visible light region.

Figure 5. (A) UV-Vis spectra and (B) Tauc plots.

Surface functional groups were analyzed by Fourier transform infrared (FTIR) spectra, as shown in Figure 6. For comparison purposes, the FTIR spectrum of the ligand used in the synthesis, 2-aminoterephthalic acid, was also included in the Figure. The peaks located at 3524 and 3410 cm^{-1} of the ligand can be assigned to the stretching of the $-\text{NH}_2$ groups [48]. In the case of the MOFs, these peaks probably are overlapped by the characteristic band of adsorbed water, situated around 3400 cm^{-1} , due to the $-\text{OH}$ stretching. Another peak related to the presence of adsorbed water was observed at 1620 cm^{-1} , assigned to the bending band of the $-\text{OH}$ group. The vibrations in the region between 1800 – 1100 cm^{-1} are related to the stretching of carboxylic, carbonyl and phenyl groups. In this sense, the stretching of the carboxylic acid group ($-\text{COOH}$, 1710 cm^{-1}) [49] presented higher intensity in the ligand precursor than in the MOFs, in which appeared in the form of a weak shoulder. This reduction in the $-\text{COOH}$ groups can be ascribed to the reaction with the metal cluster precursors, forming the structure of the MOF. Stretching of the $-\text{C}=\text{C}$ skeletal aromatic ring of the linker was observed in all synthesized samples at 1574 and 1335 cm^{-1} [50]. Vibration peaks at 1513 and 1435 cm^{-1} can be assigned to the stretching of the carbonyl asymmetric and symmetric groups from the linker, respectively [48]. In this region can also be observed the stretching of $-\text{C}-\text{N}$ (1255 cm^{-1} , characteristic of aromatic amines [50]) and the stretching vibration of $-\text{C}-\text{C}$ from the aromatic ring (1150 cm^{-1}). A last peak at 770 cm^{-1} can be associated to the out-of-plane $-\text{C}-\text{H}$ stretching [51]. The region below that peak is characterized by the vibration stretching bands (centered at 640 cm^{-1}) of $-\text{Ti}-\text{O}-\text{Ti}$ clusters and a peak at 450 cm^{-1} , corresponding to the bending vibration of these metal clusters [52]. The introduction of Zr^{4+} in the structure of the different TiZr MOFs did not show any new vibration peak but produced a reduction in the region ascribed to the vibration of the $-\text{Ti}-\text{O}-\text{Ti}$ clusters. That decrease in the intensity of the vibration was higher with increasing the molar proportion of zirconium, again confirming the successful substitution of Ti^{4+} by Zr^{4+} in the synthesis of these MOFs. Figure S2 shows the Raman spectra of the three different Ti/Zr-MOFs with successful crystalline structure. They present weak signals due to its fluorescence. The peaks at 1254 and 1422 cm^{-1} correspond to the bending and symmetric stretching of the $\text{Ti}-\text{O}-\text{Ti}-\text{O}$ framework.

This confirms that the -COOH group of the organic linker is directly connected to the Ti-oxo cluster [53]. The rest-identified peaks are associated to the organic linker. The peaks at 826 and 1126 cm^{-1} correspond to the C-H bending of the benzene ring and terephthalates rings breathing, respectively. The O=C=O symmetric stretching in carboxylate group of the organic linker appears at 1442 cm^{-1} . In contrast, the asymmetric stretching is present at 1580 cm^{-1} . On the other hand, the peak at 1278 cm^{-1} is related to the C=O stretching while 1626 cm^{-1} , to the C-C and N-H bond bending vibrations and C=C stretching of benzene ring [54,55]. In the case of TiZr15 and TiZr30 a new peak at 1592 cm^{-1} appears, probably due to the Zr incorporation.

Figure 6. FTIR spectra of Ti and TiZr MOFs (2-aminoterephthalic acid spectrum, used as ligand precursor in the synthesis of the MOFs, has also been included for comparison).

3.2. Photocatalytic tests

Before the photocatalytic tests, the adsorption capacity of the MOFs was quantified. In all cases, the adsorption equilibrium was reached in less than 1 h, describing almost negligible adsorption capacities, with ACE adsorbed amounts between 0.6 and 2% depending of the MOF. These extremely low values indicate the negligible effect of adsorption. Figure 7 represents the time-course of the ACE concentration upon solar irradiation with the synthesized Ti-Zr MOFs. In absence of photocatalyst, the ACE concentration remained constant after 6 h of irradiation, confirming the high stability of this compound under solar light. In the presence of the MOF photocatalysts two different behaviours were clearly observed. Those samples with the highest amounts of Zr (TiZr60 and TiZr80) yielded frankly poor ACE conversion, while at lower Zr proportion the incorporation of this metal improves the rate of ACE disappearance respect to the observed with the Ti MOF. These catalysts, TiZr15 and TiZr30, with a well-defined crystalline structure, allowed complete ACE degradation in less than 3 hours of irradiation in contrast with the non-crystalline materials with higher Zr content. The most promising sample, TiZr15, allowed complete ACE conversion after only 90 min of solar irradiation, probably as consequence of the optimum combination of a well-developed porosity and a lower band gap value resulting from the partial substitution of Ti^{4+} by Zr^{4+} in the structure of the MOF. Furthermore, the effect of charge recombination has also to be taken into account, as it will be shown below. The doping with Zr provides energy levels below the conduction band or above the valence band that can

act as new states for electron movements, improving the photocatalyst behaviour by decreasing the recombination of charges [56,57]. In order to verify this assumption, PL measurement were performed to investigate the recombination of photo-generated electron–hole pairs. In general, it is accepted that weak fluorescence intensity indicates a low charge recombination rate. Figure 8 represents the PL spectra of different photocatalysts. As can be seen, the incorporation of Zr into the MOF structure result in a significant decrease of the recombination, which can justify the higher photoactivity of these samples. In the case of the samples with the higher Zr content, TiZr60 and TiZr80, even lower recombinations are observed, probably due to the lower charge separation achieved with those amorphous samples.

Figure 7. Evolution of the ACE concentration under solar irradiation with the photocatalysts tested (20 °C; 250 mg·L⁻¹ of catalyst; initial acetaminophen concentration after the 1 h adsorption step \approx 5 mg·L⁻¹; intensity of irradiation: 600 W·m⁻²; pH=6.9; error bars: confidence intervals at 95%).

Figure 8. PL spectra.

We have not detected any aromatic intermediate by HPLC, probably due to their fast degradation to other organics and to the relatively low ACE initial concentration. We have also analyzed the effluent by ionic chromatography, and several short organic acids such as maleic, malonic and oxalic were detected. According to the literature [58], ACE photodegradation proceeds through the formation of hydroquinone, which undergoes oxidation to benzoquinone, which upon ring cleavage and further oxidation results in different carboxylic acids, including those detected in our study. We have also analyzed the TOC content of the water after the photocatalytic test (3 h of irradiation) when using the most active photocatalysts, TiZr15. The TOC reduction was 65.3%, indicating a significant mineralization degree. We have compared the photodegradation with TiZr15 and TiO₂ P25, which is considered the benchmark in the field (Figure S3). As can be seen in the photodegradation curves, the ZrTi15 photocatalyst shows a significant better photocatalytic

activity than that of TiO₂ P25 under solar irradiation. This result confirms the high activity ZrTi15 MOF-based photocatalyst synthesized in this study.

The rate of disappearance of ACE fitted well to a pseudo-first-order rate equation (the respective $\ln(C_0/C)$ vs. reaction time plots are shown in Figure S4 of supplementary data). The values of the apparent rate constant are given in Table 3. The highest value corresponds to TiZr15 sample, 1.7 times higher than that of the non-zirconium MOF (Ti). Since the incorporation of Zr does not lead to a considerable modification of the band gap or surface properties, this improvement in activity can be attributed to the presence of Zr ions that can act as charge trappers, leading to an increase of the charge carrier lifetimes and therefore avoiding the recombination processes and favouring the activity as supported by PL measurements (Figure 8). This effect has been also reported for other metal-doped semiconductors [26,59]. For the sake of comparison with other photocatalysts previously reported by our research group, tested under the same conditions, the photonic efficiency (ξ) has been determined following to the Serpone's method [60], considering the photon flux in these experiments equal to $6.38 \cdot 10^{-3}$ mol photon \cdot min⁻¹. The data for all synthesized MOFs are collected in Table 3. TiZr15 yielded a photonic efficiency of 1.89 einstein⁻¹, much higher than the obtained for the solar photocatalytic degradation of antipyrine with Zr-doped TiO₂ supported on delaminated clay photocatalysts (1.2 einstein⁻¹) [26], and those of TiO₂-ZnO/clay materials for the degradation of acetaminophen under solar light whose maximum value reached 1.0 einstein⁻¹ [61]. Even, the Ti and TiZr30 samples were more efficient than previous reported catalysts. Thus, these new mixed Ti-Zr metal organic frameworks appear promising photocatalysts for the removal of water pollutants using solar light as energy source. Table 4 summarizes the highest photocatalytic degradation rate of acetaminophen obtained in this study with other previously reported, all of them obtained under solar irradiation. The highest rate constant, 0.0121 min⁻¹, is much higher than that previously reported by our research group for the solar photocatalytic degradation of antipyrine with Zr-doped TiO₂ supported on delaminated clay photocatalysts (0.0098 min⁻¹) [26]. We also reported on the photodegradation of acetaminophen under solar light with ZnO/sepiolite [62] and Ag/ZnO-TiO₂/clay heterostructures [63]. The maximum values of the pseudo first-order rate constant were 0.0032 and 0.0095 min⁻¹, respectively, also bellow than the obtained with the best photocatalysts described in the current work. Jallouli et al. [64] reported a slight

lower rate constant using TiO₂/cellulosic fibers photocatalysts. However, higher rate constants were reported when using Pt/TiO₂ [58] and C-modified TiO₂ [65] photocatalysts.

Table 3. Values of the pseudo-first order rate constant of ACE disappearance under solar irradiation with the catalysts tested.

Table 4. Comparison of pseudo-first order rate constants of ACE disappearance.

Regarding the optimal parameters of reaction with TiZr15, different tests were carried out to analyze the effects of the initial photocatalyst dosage and the initial pH on the ACE photodegradation. The evolution of the acetaminophen concentrations at different photocatalyst loadings are depicted in Figure 9. The best results in terms of photocatalytic activity were obtained with a 250 mg·L⁻¹ TiZr dosage. The increase of the photocatalyst dosage beyond this point results in the decrease of the photodegradation of ACE, probably as a consequence of the poorer penetration of light within the solution. Another important parameter of the reaction is the initial pH of the solution. The results obtained for different initial pH in the range 3 to 11 using TiZr15 as photocatalyst can be observed in Figure 10. In acidic medium (pH ≤ 5), the performance of the TiZr15 was remarkably reduced. This can be ascribed to the scavenging effect over the O₂^{•-} (the main specie involved in the oxidation of the ACE, as shown below in Figure 11) by protons, resulting in the formation of the hydroperoxide radical (HO₂[•], with a lower oxidant power compared to O₂^{•-} [66]). A lower conversion of ACE was also obtained in strong basic medium (pH = 11), due to the degradation of the catalyst. In this sense, the characteristic yellow-colored TiZr15 sample was turned into a lighter color when the reaction was carried out at an initial pH of 11. From these results, it can be concluded that a catalyst dose of 250 mg·L⁻¹ and neutral or slight basic initial pH are the more suitable conditions for the best performance of the TiZr15 MOF.

Figure 9. Evolution of ACE concentration under solar light at different initial TiZr15 dosages (20 °C; initial ACE concentration ≈ 5 mg·L⁻¹; intensity of irradiation: 600 W·m⁻²; pH=6.9).

Figure 10. Evolution of ACE concentration under solar light with TiZr15 at different initial pH (20 °C; 250 mg·L⁻¹ of catalyst; initial acetaminophen concentration after adsorption \approx 5 mg·L⁻¹; intensity of irradiation: 600 W·m⁻²).

To learn on the reactive species involved in the photodegradation process, tests with different scavengers (IPA, p-BQ, KI or AgNO₃) were carried out, using the most active photocatalyst TiZr15. Isopropanol (IPA) was used to trap the hydroxyl radicals (\cdot OH) [67], benzoquinone (p-BQ) for the superoxide radicals ($O_2^{\cdot-}$) [68], potassium iodide (KI) as electron (e^-) acceptor, while silver nitrate (AgNO₃) was used for holes (h^+) [69,70]. In all cases, the scavenger was used at 1 mM concentration, without modifying any other reaction condition. Figure 11A shows the evolution of ACE concentration upon irradiation time in presence of different scavengers at 1 mM starting concentration. The values of the pseudo-first order rate constants of ACE disappearance are also included (Figure 11B). It can be observed that the addition of KI, a hole scavenger, had no significant effect, being the results almost similar to the obtained in the absence of this scavenger. This suggests a negligible participation of holes in the photodegradation of ACE. In contrast, the rate of photocatalytic decomposition of ACE decreased in different extents with the addition of IPA, AgNO₃ and p-BQ, \cdot OH, electron and $O_2^{\cdot-}$ scavengers, respectively. The last showed the most pronounced effect, suggesting that $O_2^{\cdot-}$ is the main contributing radical in the photocatalytic process investigated with the TiZr MOF tested. It is important to remark that the behaviour of the different oxidizing species might vary depending on the pollutant-photocatalyst system and the solution pH. For example, the degradation of rhodamine B dye has been reported to be primarily due to $O_2^{\cdot-}$ and h^+ with both Bi₂MoO₆/UiO-66(Zr) [71] and BiOBr/NH₂-MIL-125(Ti) [19] photocatalysts. In contrast, $O_2^{\cdot-}$ and \cdot OH were the main contributing species in the photodegradation of this dye with Ag/MIL-125 as photocatalyst [17]. \cdot OH radicals are considered the dominant oxidizing species in a wide range of photocatalytic reactions, including the oxidation of pharmaceuticals [61,63]. Nevertheless, our results point to $O_2^{\cdot-}$ as the main responsible in this case (pH₀=6.9). These species can be generated by the interaction of photogenerated electrons with O₂ adsorbed at the MOF surface.

Figure 11. (A) ACE concentration profiles upon irradiation time and (B) values of the pseudo-first order rate constant of ACE disappearance (k) with TiZr15 photocatalyst using different scavengers at 1 mM initial concentration. Operating conditions as in Figure 7.

The stability and reusability of the photocatalyst is a crucial issue regarding potential applications. The stability of the best photocatalyst was checked upon three successive runs. In each cycle, the dispersion was maintained under stirring in dark for 1 h and then was exposed to solar light irradiation for 3 h. Then, the photocatalyst was separated by filtration and simply washed with distilled water and dried at 60 °C prior use in the following run. The reaction conditions were the same as those described before. Figure 12 represents the ACE conversion achieved after 3 h of solar irradiation in the three successive runs with TiZr15. The photocatalytic activity decreased slightly after the first cycle and then remained almost unchanged from the second to the third runs, in which conversion values above 90% were maintained. After the third use the catalyst was characterized by XRD and SEM (Figure 13). Additionally, N₂ adsorption-desorption isotherm (Figure S5) and WDXRF (Table S1) were also carried out. The diffraction pattern remained almost unchanged with no apparent displacement of the characteristic diffraction peaks and without additional ones. No significant morphological changes were observed from the SEM images of the used catalyst (Figure 13B) respect to the first one (Figure 2B). There are no notable changes in the N₂ isotherm shape (Figure S5) nor in the chemical composition (Table S1), just the surface area suffered a slight decrease, from 1036 to 930 m²·g⁻¹, probably due to the presence of adsorbed molecules that blockage part of the porous network. Thus, TiZr15 appears as a promising photocatalyst for degradation of emerging contaminants with a high stability.

Figure 12. ACE conversion after 3 h of solar irradiation upon three successive runs with TiZr15. Operating conditions as Figure 7.

Figure 13. XRD pattern (A) and SEM image (B) of TiZr15 after the three successive runs.

4. Conclusions

Mixed Ti-Zr MOFs based on NH₂-MIL-125 were successfully synthesized with different Ti:Zr molar ratios within a wide range. At low to moderate Zr proportions these materials show the same crystalline structure that NH₂-MIL-125, although with a higher average crystal size and an expanded unit cell, due to the substitution of Ti⁴⁺ by Zr⁴⁺. They show high surface area values and essentially microporous texture. Nevertheless, at higher Zr amounts materials with amorphous structure and much lower porosity were obtained. The crystalline TiZr15

yielded the highest activity for the solar photocatalytic degradation of acetaminophen, even higher than that of the non-zirconium MOF, allowing complete ACE conversion after 90 min, well below the reaction time required with other catalysts tested by our group in previous works [26,61,63]. PL measurements indicate that the incorporation of Zr into the MOF structure results in a significant decrease of the recombination, which can justify the higher photoactivity of these samples. Experiments with scavengers lead to the conclusion that $O_2^{\cdot-}$ is the main contributing species in the photodegradation of ACE, although photogenerated $\cdot OH$ radicals and electrons are also partly involved. TiZr15 remains fairly stable after three successive runs, maintaining its crystalline structure and morphology unchanged and allowing more than 90% ACE conversion under the operating conditions tested.

Acknowledgements

The authors acknowledge the financial support from Spanish MINECO (project CTQ2016-78576-R). M. Peñas-Garzón thanks Spanish MECD for FPU16/00576 grant. Authors thank the Research Support Services of the University of Extremadura (SAIUEx) for its technical and scientific support. We also thank to Dr. Juan Cabanillas for his help with PL measurements.

References

- [1] J. Qiu, X. Zhang, Y. Feng, X. Zhang, H. Wang, J. Yao, Modified metal-organic frameworks as photocatalysts, *Appl. Catal. B: Environ.* 231 (2018) 317-342.
- [2] M.B. Chambers, X. Wang, L. Ellezam, O. Ersen, M. Fontecave, C. Sanchez, L. Rozes, C. Mellot-Draznieks, Maximizing the photocatalytic activity of metal-organic frameworks with aminated-functionalized linkers: Substoichiometric effects in MIL-125-NH₂, *J. Am. Chem. Soc.* 139 (2017) 8222–8228.
- [3] H. Furukawa, N. Ko, Y.B. Go, N. Aratani, S.B. Choi, E. Choi, A.Ö. Yazaydin, R.Q. Snurr, M. O’Keeffe, J. Kim, O.M. Yaghi, Ultrahigh porosity in metal-organic frameworks. *Sci.* 329 (2010) 424-428.
- [4] B. Szczeńśniak, J. Choma, M. Jaroniec, Gas adsorption properties of hybrid graphene-MOF materials, *J. Colloid Interface Sci.* 514 (2018) 801-813.

- [5] Q.-G. Zhai, N. Bai, S. Li, X. Bu, P. Feng, Design of Pore Size and Functionality in Pillar-Layered Zn-Triazolate-Dicarboxylate Frameworks and Their High CO₂/CH₄ and C₂ Hydrocarbons/CH₄ Selectivity. *Inorg. Chem.* 54 (2015) 9862-9868.
- [6] A.R. Millward, O.M. Yaghi, Metal-organic frameworks with exceptionally high capacity for storage of carbon dioxide at room temperature, *J. Am. Chem. Soc.* 127 (2005) 17998-17999.
- [7] G.-Y. Zhang, C. Cai, S. Cosnier, H.-B. Zheng, X.-J. Zhang, D. Shan, Zirconium-metalloporphyrin frameworks as a three-in-one platform possessing oxygen nanocage, electron media, and bonding site for electrochemiluminescence protein kinase activity assay, *Nanoscale* 8 (2016) 11649-11657.
- [8] V. Stavila, A.A. Talin, M.D. Allendorf, MOF-based electronic and opto-electronic devices, *Chem. Soc. Rev.* 43 (2014) 5994-6010.
- [9] W. Li, Y. Zhang, Q. Li, G. Zhang, Metal-organic framework composite membranes: Synthesis and separation applications. *Chem. Eng. Sci.* 135 (2017) 232-257.
- [10] S. Qiu, M. Xue, G. Zhu, Metal-organic framework membranes: from synthesis to separation application, *Chem. Soc. Rev.* 43 (2014) 6116-6140.
- [11] N.A. Khan, Z. Hasan, S.H. Jhung, Adsorptive removal of hazardous materials using metal-organic frameworks (MOFs): A review. *J. Hazard. Mater.* 244-245 (2013) 444-456.
- [12] C.-C. Wang, J.-R. Li, X.-L. Lv, Y.-Q. Zhang, G. Guo, Photocatalytic organic pollutants degradation in metal-organic frameworks. *Energ. Environ. Sci.* 7 (2014) 2831-2867.
- [13] Z.-T. Yu, Z.-L. Liao, Y.-S. Jiang, G.-H. Li, G.-D. Li, J.-S. Chen, Construction of a microporous inorganic-organic hybrid compound with uranyl units, *Chem. Comm.* 10 (2004) 1814-1815.
- [14] P. Mahata, G. Madras, S. Natarajan, Novel photocatalysts for the decomposition of organic dyes based on metal-organic framework compounds, *J. Phys. Chem. B* 110 (2006) 13759-13768.
- [15] L. Chen, R. Luque, Y. Li, Controllable design of tunable nanostructures inside metal-organic frameworks. *Chem. Soc. Rev.* 46 (2017) 4614-4630.
- [16] C. Yang, X. You, J. Cheng, H. Zheng, Y. Chen, A novel visible-light-driven In-based MOF/graphene oxide composite photocatalyst with enhanced photocatalytic activity toward the degradation of amoxicillin, *Appl. Catal. B Environ.* 200 (2017) 673-680.

- [17] H. Guo, D. Guo, Z. Zheng, W. Weng, J. Chen, Visible-light photocatalytic activity of Ag@MIL125(Ti) microspheres, *Appl. Organometal. Chem.* 29 (2015) 618–623.
- [18] M. Dan-Hardi, C. Serre, T. Frot, L. Rozes, G. Maurin, C. Sanchez, G. Férey, A new photoactive crystalline highly porous titanium(IV) dicarboxylate, *J. Am. Chem. Soc.* 131 (2009) 10857-10859.
- [19] S.-R. Zhu, P.-F. Liu, M.-K. Wu, W.-N. Zhao, G.-C. Li, K. Tao, F.-Y. Yi, L. Han, Enhanced photocatalytic performance of BiOBr/NH₂-MIL-125(Ti) composite for dye degradation under visible light, *Dalton Trans.* 45 (2016) 17521-17529.
- [20] R.M. Abdelhameed, A.M.S. Silva, J. Rocha, Enhanced photocatalytic activity of MIL-125 by post-synthetic modification with Cr(III) and Ag nanoparticles. *Chem. A Eur. J.* 21 (2015) 11072-11081.
- [21] J. G. Santaclara, M. A. Nasalevich, S. Castellanos, W.H. Evers, F.C.M. Spoor, K. Rock, L.D.A. Siebbeles, F. Kapteijn, F. Grozema, A. Houtepen, J. Gascon, J. Hunger, M.A. van der Veen, Organic Linker Defines the Excited- State Decay of Photocatalytic MIL- 125(Ti)- Type Materials, *Chem. Sus. Chem.* 9 (2016) 388-395.
- [22] M. de Miguel, F. Ragon, T. Devic, C. Serre, P. Horcajada, H. García, Evidence of photoinduced charge separation in the metal-organic framework MIL-125(Ti)-NH₂, *Chem. Phys. Chem.* 13 (2012) 3651-3658.
- [23] J.H. Cavka, S. Jakobsen, U. Olsbye, N. Guillou, C. Lamberti, S. Bordiga, K.P. Lillerud, A new zirconium inorganic building brick forming metal organic frameworks with exceptional stability, *J. Am. Chem. Soc.* 130 (2008) 13850-13851.
- [24] B. Wang, X.-L., Lv, D. Feng, L.-H. Xie, J. Zhang, M. Li, Y. Xie, J.-R. Li, H.-C. Zhou, Highly stable Zr(IV)-based metal-organic frameworks for the detection and removal of antibiotics and organic explosives in water, *J. Am. Chem. Soc.* 138 (2016) 6204-6216.
- [25] G. Férey, C. Mellot-Draznieks, C. Serre, F. Millange, J. Dutour, S. Surble, I. Margiolaki, A chromium terephthalate-based solid with unusually large pore volumes and surface area. *Sci.* 309 (2005) 2040-2042.
- [26] C. Belver, J. Bedia, J.J. Rodriguez, Zr-doped TiO₂ supported on delaminated clay materials for solar photocatalytic treatment of emerging pollutants, *J. Hazard. Mat.* 322 (2017) 233–242.

- [27] J. Rivera-Utrilla, M. Sánchez-Polo, M.A. Ferro-García, G. Prados-Joya, R. Ocampo-Pérez, Pharmaceuticals as emerging contaminants and their removal from water. A review. *Chemosphere* 93 (2013) 1268–1287.
- [28] P. Amrita, K. Yew-Hoong Gin, A. Yu-Chen Lin, M. Reinhard, Impacts of emerging contaminants on freshwater resources: review of recent occurrences, sources, fate and effects, *Sci. Total Environ.* 408 (2010) 6062–6069.
- [29] Y. Lee, S. Kim, J. Kang, S.M. Cohen, Photocatalytic CO₂ reduction by a mixed metal (Zr/Ti), mixed ligand metal–organic framework under visible light irradiation, *Chem. Commun.* 51 (2015) 5735–5738.
- [30] H. Wang, X. Yuan, Y. Wu, G. Zeng, X. Chen, L. Leng, Z. Wu, L. Jiang, H. Li, Facile synthesis of amino-functionalized titanium metal-organic frameworks and their superior visible-light photocatalytic activity for Cr(VI) reduction, *J. Hazard. Mater.* 286 (2015) 187–194.
- [31] Z. Wu, X. Huang, H. Zheng, O. Wabg, G. Hai, W. Dong, G. Wang, Aromatic heterocycle-grafted NH₂-MIL-125(Ti) via conjugated linker with enhanced photocatalytic activity for selective oxidation of alcohols under visible light. *Appl. Catal. B Environ.* 224 (2018) 479–487.
- [32] Y. Fu, L. Sun, H. Yang, L. Xu, F. Zhang, W. Zhu, Visible-light-induced aerobic photocatalytic oxidation of aromatic alcohols to aldehydes over Ni-doped NH₂-MIL-125(Ti), *Appl. Catal. B Environ.* 187 (2016) 212–217.
- [33] D. Sun, L. Ye, Z. Li, Visible-light-assisted aerobic photocatalytic oxidation of amines to imines over NH₂-MIL-125(Ti), *Appl. Catal. B Environ.* 164 (2015) 428–432.
- [34] S. Hu, M. Liu, K. Li, C. Song, G. Zhang, X. Guo, Surfactant-assisted synthesis of hierarchical NH₂-MIL-125 for the removal of organic dyes, *RSC Adv.* 7 (2017) 581–587.
- [35] M. Martis, W. Meicheng, K. Mori, H. Yamashita, Fabrication of metal nanoparticles in metal organic framework NH₂-MIL-125 by UV photo-assisted methods for optimized catalytic properties, *Catal. Today* 235 (2014) 98–102.
- [36] T.J.B. Holland, S.A.T. Redfern, Unit cell refinement from powder diffraction data: the use of regression diagnostics, *Miner. Mag.* 61 (1997) 6577.
- [37] J. Landers, G.Y. Gor, A.V. Neimark, Density functional theory methods for characterization of porous materials, *Colloids Surf. A: Physicochem. Eng. Asp.* 437 (2013) 3–32.

- [38] J. Zhang, P. Zhou, J. Liu, J. Yu, New understanding of the difference of photocatalytic activity among anatase, rutile and brookite TiO₂, *Phys. Chem. Chem. Phys.* 16 (2014) 20382–20386.
- [39] J. Tauc, Absorption edge and internal electric fields in amorphous semiconductors, *Mater. Res. Bull.* 5 (1970) 721–726.
- [40] S.N. Kim, J. Kim, H.Y. Kim, H.Y. Cho, W.S. Ahn, Adsorption/catalytic properties of MIL-125 and NH₂-MIL-125, *Catal. Today* 204 (2013) 85–93.
- [41] D. Sun, W. Liu, M. Qiu, Y. Zhang, Z. Li, Introduction of a mediator for enhancing photocatalytic performance via post-synthetic metal exchange in metal-organic frameworks (MOFs), *Chem. Comm.* 51 (2015) 2056-2059.
- [42] C.H. Hendon, D. Tiana, M. Fontecave, C. Sanchez, L. D'Arras, C. Sassoey, L. Rozes, C. Mellot-Draznieks, A. Walsh, Engineering the optical response of the titanium-MIL-125 metal-organic framework through ligand functionalization. *J. Am. Chem. Soc.* 135 (2013) 10942-10945.
- [43] Y.-F. Li, D. Xu, J.I. Oh, W. Shen, X. Li, Y. Yu, Mechanistic study of codoped titania with nonmetal and metal ions: A case of C-Mo Codoped TiO₂, *ACS Catal.* 2 (2012) 391-398.
- [44] Y.-H. Fan, S.-W. Zhang, S.-B. Qin, X.-S. Lia, S.-H. Qia, An enhanced adsorption of organic dyes onto NH₂ functionalization titanium-based metal-organic frameworks and the mechanism investigation, *Microp. Mesop. Mater.* 263 (2018) 120-127.
- [45] M. Oveisi, M. Alina Asli, N. Mohammad Mahmoodi, MIL-Ti metal-organic frameworks (MOFs) nanomaterials as superior adsorbents: Synthesis and ultrasound-aided dye adsorption from multicomponent wastewater systems, *J. Hazard. Mater.* 347 (2018) 123–140.
- [46] C. Zlotea, D. Phanon, M. Mazaj, D. Heurtaux, V. Guillermin, C. Serre, P. Horcajada, T. Devic, E. Magnier, F. Cuevas, G. Férey, P.L. Llewellyn, M. Latroche, Effect of NH₂ and CF₃ functionalization on the hydrogen sorption properties of MOFs, *Dalton Trans.* 40 (2011) 4879–4881.
- [47] J. Bedia, V. Muelas-Ramos, M. Peñas-Garzón, A. Gómez-Avilés, J.J. Rodríguez, C. Belver. A review on the synthesis and characterization of metal organic frameworks for photocatalytic water purification, *Catalysts*, 9 (2019) 52–95.
- [48] S. Hu, M. Liu, K. Li, Y. Zuo, A. Zhang, C. Song, G. Zhang, X. Guo, X, Solvothermal synthesis of NH₂-MIL-125(Ti) from circular plate to octahedron, *Cryst. Eng. Comm.* 16 (2014) 9645–9650.

- [49] D. Mohan, K.P. Singh, S. Sinha, D. Gosh, Removal of pyridine from aqueous solution using low cost activated carbons derived from agricultural waste materials, *Carbon* 42 (2004) 2409–2421.
- [50] M. Oveisi, M.A. Asli, N.M. Mahmoodi, MIL-Ti metal-organic frameworks (MOFs) nanomaterials as superior adsorbents: Synthesis and ultrasound-aided dye adsorption from multicomponent wastewater systems, *J. Hazard. Mater.* 347 (2018) 123–140.
- [51] J. Bedia, R. Barrionuevo, J. Rodríguez-Mirasol, T. Cordero, Ethanol dehydration to ethylene on acid carbon catalysts, *Appl. Catal. B Environ.* 103 (2011) 302–310.
- [52] M. Shafaei, E.K. Goharshadi, M. Mashreghi, M. Sadeghinia, TiO₂ nanoparticles and TiO₂@graphene quantum dots nanocomposites as effective visible/solar light photocatalysts, *J. Photochem. Photobiol. A Chem.* 357 (2018) 90–102.
- [53] P. Karthik, R. Vinoth, P. Zhang, W. Choi, E. Balaraman, B. Neppolian, π - π interaction between metal-organic framework and reduced graphene oxide for visible-light photocatalytic H₂ production, *ACS Appl. Energy Mater.* 1 (2018) 1913–1923.
- [54] I. Strauss, A. Mundstock, D. Hinrichs, R. Himstedt, A. Knebel, C. Reinhardt, D. Dorfs, J. Caro, The interaction of guest molecules with Co-MOF-74: A Vis/NIR and Raman approach, *Angew. Chemie - Int. Ed.* 57 (2018) 7434–7439.
- [55] C. Atzori, G.C. Shearer, L. Maschio, B. Civalleri, F. Bonino, C. Lamberti, S. Svelle, K.P. Lillerud, S. Bordiga, Effect of benzoic acid as a modulator in the structure of UiO-66: An experimental and computational study, *J. Phys. Chem. C* 121 (2017) 9312–9324.
- [56] F. Fresno, M.D. Hernández-Alonso, D. Tudela, J.M. Coronado, J. Soria, Photocatalytic degradation of toluene over doped and coupled (Ti,M)O₂ (M = Sn or Zr) nanocrystalline oxides: Influence of the heteroatom distribution on deactivation, *Appl. Catal. B: Environ.* 84 (2008) 598–606.
- [57] J. Lukác, M. Klementová, P. Bezdieka, S. Bakardjieva, J. Subrt, L. Szatmáry, Z. Bast, J. Jirkovsky, Influence of Zr as TiO₂ doping ion on photocatalytic degradation of 4-chlorophenol, *Appl. Catal. B* 74 (2007) 83–91.
- [58] O. Nasr, O. Mohamed, A.-S. Al-Shirbini, A.-M. Abdel-Wahab, Photocatalytic degradation of acetaminophen over Ag, Au and Pt loaded TiO₂ using solar light, *J. Photochem. Photobiol. A: Chem.* 374 (2019) 185–193.
- [59] P. Bouras, E. Stathatos, P. Lianos, Pure versus metal-ion-doped nanocrystalline titania for photocatalysis, *Appl. Catal. B: Environ.* 73 (2007) 51–59.

- [60] N. Serpone, Relative photonic efficiencies and quantum yields in heterogeneous photocatalysis, *J. Photochem. Photobiol. A* 104 (1997) 1-12.
- [61] M. Tobajas, C. Belver, J.J. Rodriguez, Degradation of emerging pollutants in water under solar irradiation using novel TiO₂-ZnO/clay nanoarchitectures, *Chem. Eng. J.* 309 (2017) 596–606.
- [62] M. Akkari, P. Aranda, C. Belver, J. Bedia, A. Ben Haj Amara, E. Ruiz-Hitzky, ZnO/sepiolite heterostructured materials for solar photocatalytic degradation of pharmaceuticals in wastewater, *Appl. Clay Sci.* 156 (2018) 104-109.
- [63] C. Belver, M. Hinojosa, J. Bedia, M. Tobajas, M.A. Alvarez, V. Rodríguez-González, J.J. Rodriguez, Ag-coated heterostructures of ZnO-TiO₂/delaminated montmorillonite as solar photocatalysts, *Materials* 10 (2017) 960-977.
- [64] N. Jallouli, K. Elghniji, H. Trabelsi, M. Ksibi, Photocatalytic degradation of paracetamol on TiO₂ nanoparticles and TiO₂/cellulosic fiber under UV and sunlight irradiation, *Arabian Journal of Chemistry* 10 (2017) S3640-S3645.
- [65] A. Gómez-Avilés, M. Peñas-Garzón, J. Bedia, J.J. Rodriguez, C. Belver, C-modified TiO₂ using lignin as carbon precursor for the solar photocatalytic degradation of acetaminophen, *Chem. Eng. J.* 358 (2019) 1574-1582.
- [66] E. Brillas, I. Sirés, M.A. Oturan, Electro-fenton process and related electrochemical technologies based on fenton's reaction chemistry, *Chem. Rev.* 109 (2009) 6570–6631.
- [67] L. Ye, J.Y. Liu, Z. Jiang, T.Y. Peng, L. Zan, Facets coupling of BiOBr-g-C₃N₄ composite photocatalyst for enhanced visible-light-driven photocatalytic activity, *Appl. Catal. B Environ.* 142 (2013) 1–7.
- [68] M.C. Yin, Z.S. Li, J.H. Kou, Z.G. Zou, Mechanism investigation of visible light-induced degradation in a heterogeneous TiO₂/Eosin Y/Rhodamine B system, *Environ. Sci. Technol.* 43 (2009) 8361–8366.
- [69] G. Li, K.H. Wong, X. Zhang, C. Hu, J.C. Yu, R.C.Y. Chan, P.K. Wong, Degradation of Acid Orange 7 using magnetic AgBr under visible light: The roles of oxidizing species. *Chemosphere* 76 (2009) 1185-1191.
- [70] Q.B. Li, X. Zhao, J. Yang, C.J. Jia, Z. Jin, W.L. Fan, Exploring the effects of nanocrystal facet orientations in g-C₃N₄/BiOCl heterostructures on photocatalytic performance, *Nanoscale* 7 (2015) 18971–18983.

[71] J. Ding, Z. Yang, C. He, X. Tong, Y. Li, X. Niu, H. Zhang, UiO-66(Zr) coupled with Bi_2MoO_6 as photocatalyst for visible-light promoted dye degradation, J. Colloid Interface Sci. 497 (2017) 126-133.

Table 1. Structural parameters of the synthesized Ti-Zr MOFs.

Sample	D (nm) ^a	<i>a</i> (Å) ^b	<i>b</i> (Å) ^b	<i>c</i> (Å) ^b	<i>V</i> (Å ³) ^b
Ti	32.2	19.244	21.358	38.181	15693
TiZr15	34.7	26.904	21.445	39.184	22607
TiZr30	34.4	26.749	21.453	39.079	22426

^a Average crystal size calculated by Scherrer’s formula with the (121) reflection. ^b Unit cell parameters and cell volume refined by the UnitCell software.

Table 2. Porous texture and band gap values.

	Porous texture parameters					Band Gap
	S _{BET} (m ² /g)	S _{MP} (m ² /g)	S _{EXT} (m ² /g)	V _{MP} (cm ³ /g)	V _T (cm ³ /g)	E _g (eV)
Ti	1048	1007	42	0.49	0.56	2.74
TiZr15	1036	986	50	0.42	0.52	2.70
TiZr30	821	758	63	0.33	0.45	2.64
TiZr60	129	66	64	0.03	0.13	2.65
TiZr80	275	215	61	0.09	0.20	2.71

Table 3. Values of the pseudo-first order rate constant of ACE disappearance (*k*) and photonic efficiency (ξ) under solar irradiation with the catalysts tested.

Catalyst	<i>k</i> (min ⁻¹)	photonic efficiency (ξ , einstein ⁻¹)
Ti	0.0073	1.14
TiZr15	0.01214	1.89
TiZr30	0.01057	1.66
TiZr60	0.00247	0.39
TiZr80	0.00251	0.39

Table 4. Comparison of pseudo-first order rate constants of ACE disappearance.

Catalyst	k (min ⁻¹)	Reference
TiZr15	0.0121	This work
Zr-doped TiO ₂ on clay	0.0098	[26]
ZnO/sepiolite	0.0032	[62]
Ag/ZnO-TiO ₂ /clay heterostructures	0.0095	[63]
Pt/TiO ₂	0.0260	[53]
C-modified TiO ₂	0.0670	[65]
TiO ₂ /cellulosic fibers	0.0110	[64]

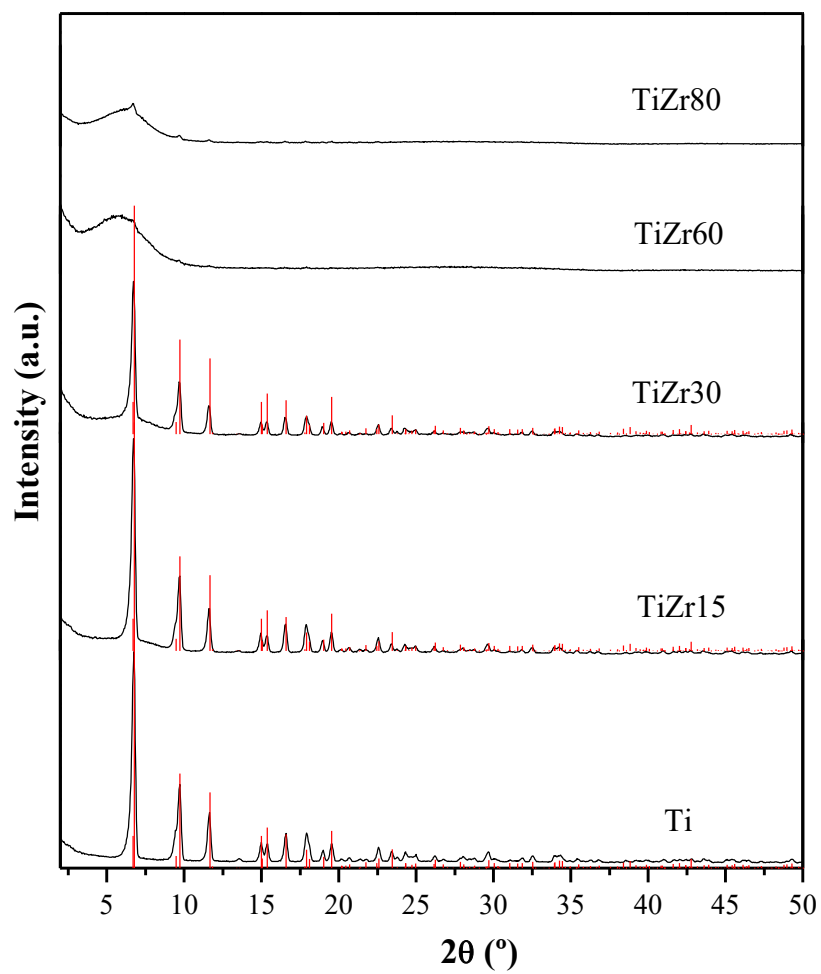


Figure 1. XRD patterns. The characteristic peaks of the MIL-125 (ref. ja903726m_si_002.cif [18]) are included as reference (red colour).

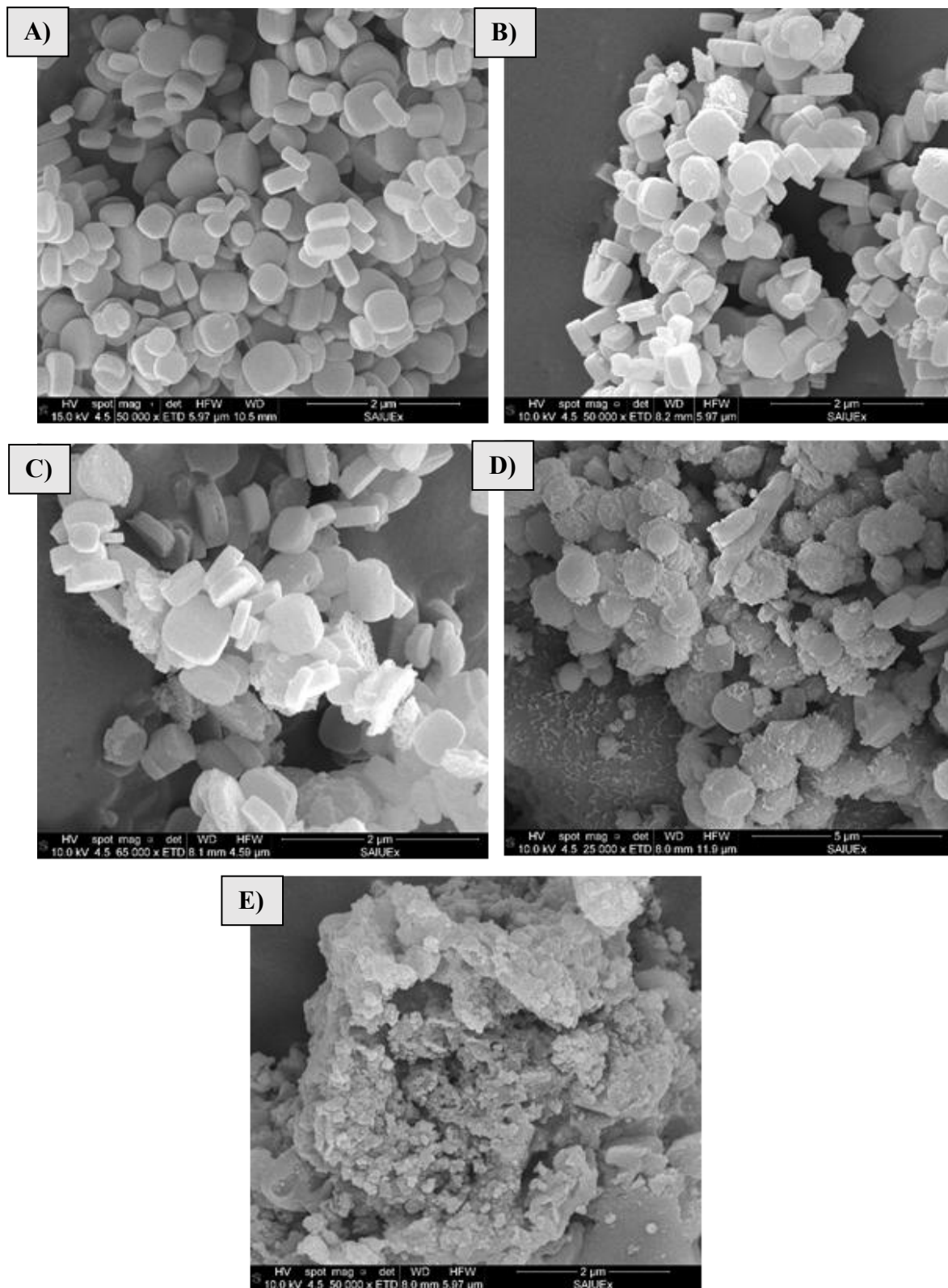


Figure 2. SEM images of (A) Ti, (B) TiZr15, (C) TiZr30, (D) TiZr60 and (E) TiZr80.

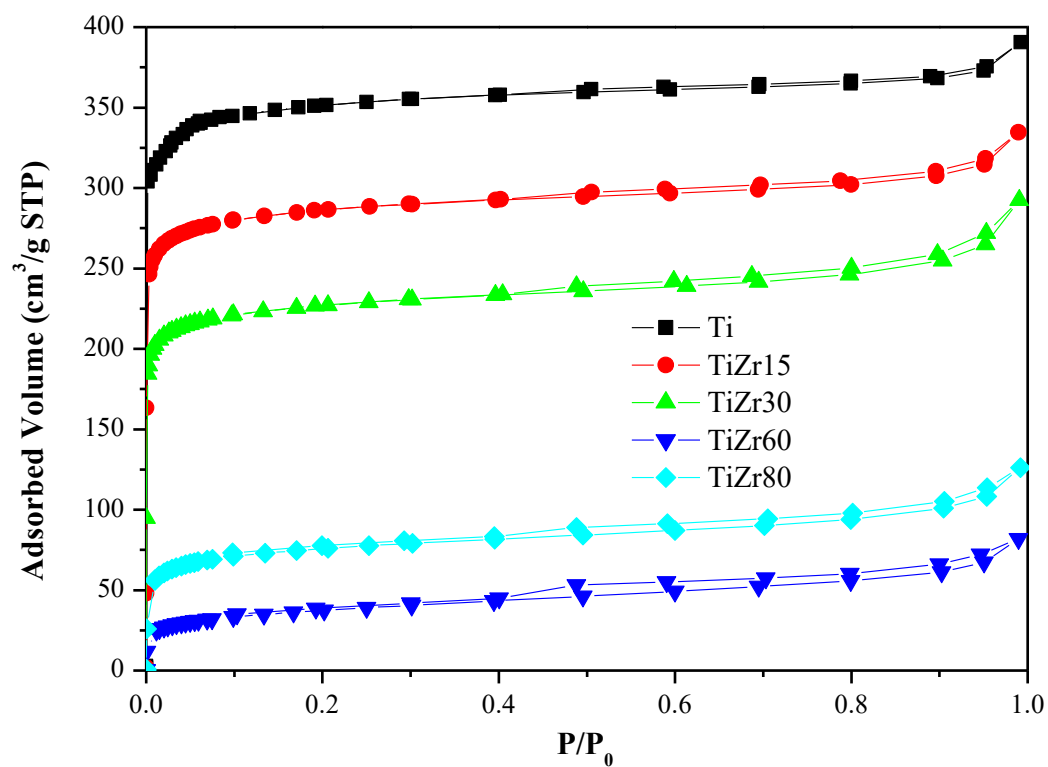


Figure 3. Nitrogen adsorption–desorption isotherms at -196 °C.

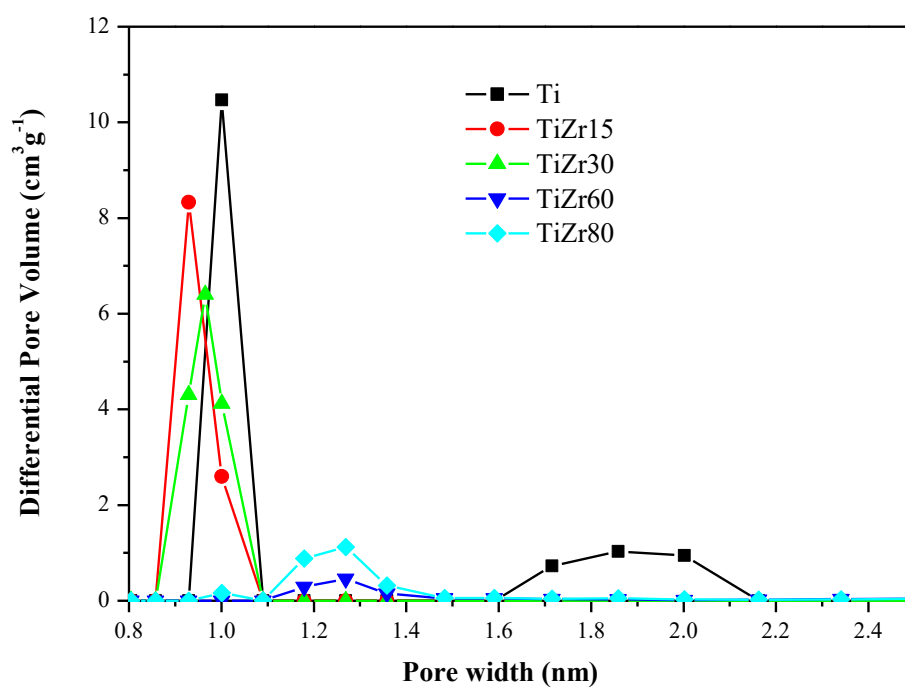


Figure 4. DFT pore size distributions.

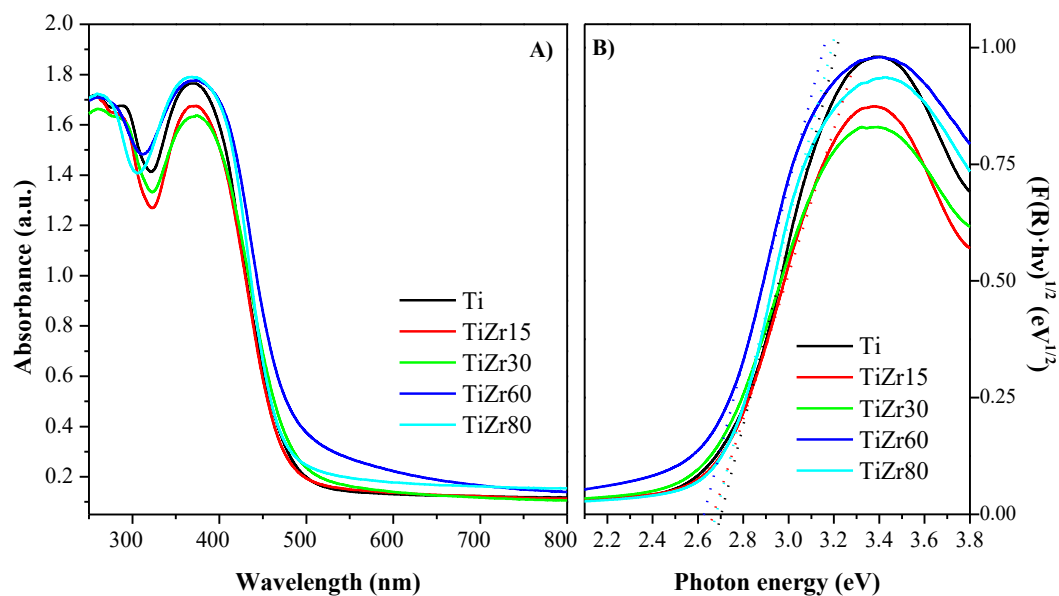


Figure 5. (A) UV-Vis spectra and (B) Tauc plots.

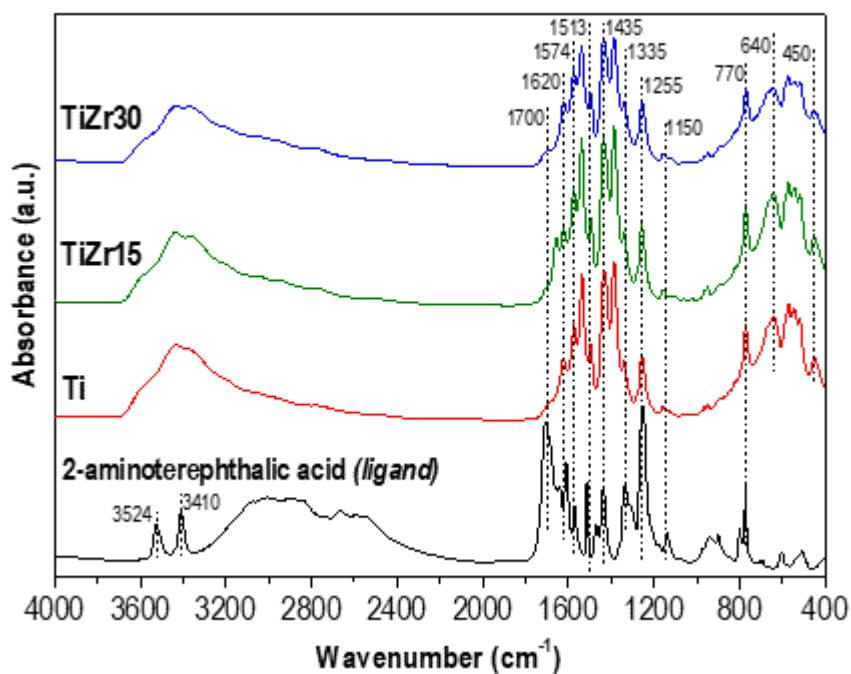


Figure 6. FTIR spectra of Ti and TiZr MOFs (2-aminoterephthalic acid spectrum, used as ligand precursor in the synthesis of the MOFs, has also been included for comparison).

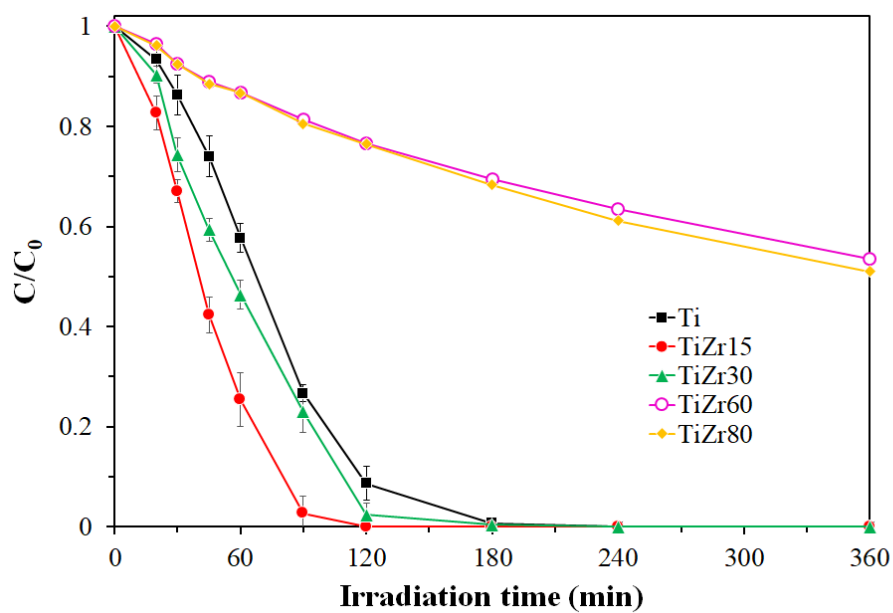


Figure 7. Evolution of the ACE concentration under solar irradiation with the photocatalysts tested (20 °C; 250 mg·L⁻¹ of catalyst; initial acetaminophen concentration after the 1 h adsorption step \approx 5 mg·L⁻¹; intensity of irradiation: 600 W·m⁻²; pH=6.9; error bars: confidence intervals at 95%).

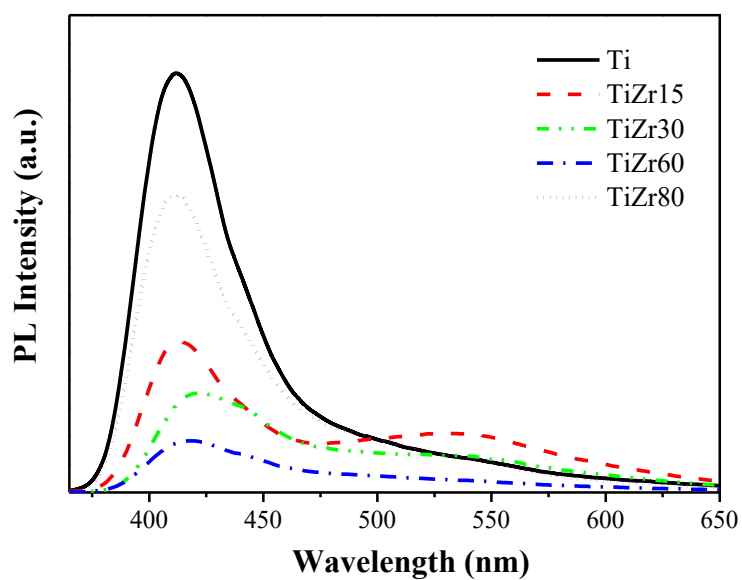


Figure 8. PL spectra.

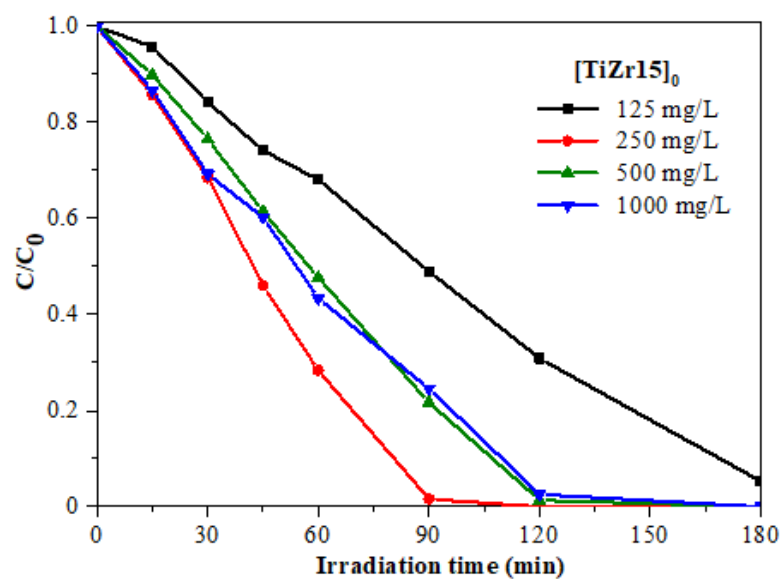


Figure 9. Evolution of ACE concentration under solar light at different initial TiZr15 dosages (20 °C; initial ACE concentration $\approx 5 \text{ mg}\cdot\text{L}^{-1}$; intensity of irradiation: $600 \text{ W}\cdot\text{m}^{-2}$; pH=6.9).

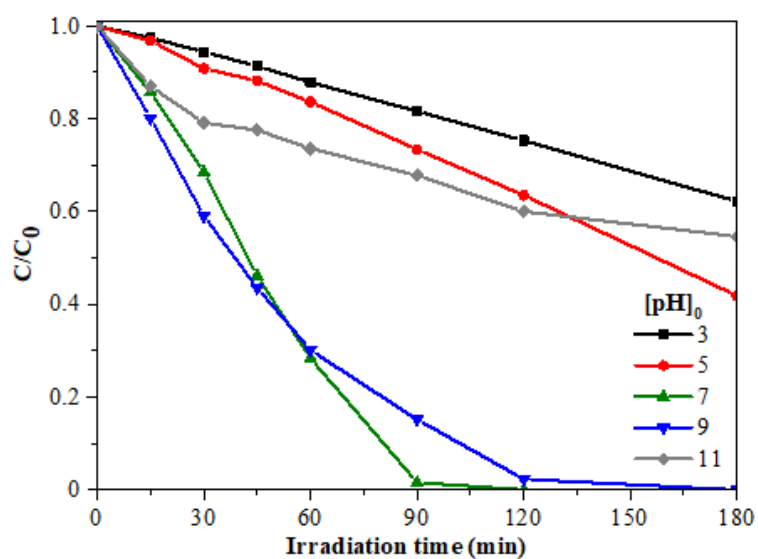


Figure 10. Evolution of ACE concentration under solar light with TiZr15 at different initial pH (20 °C; $250 \text{ mg}\cdot\text{L}^{-1}$ of catalyst; initial acetaminophen concentration after adsorption $\approx 5 \text{ mg}\cdot\text{L}^{-1}$; intensity of irradiation: $600 \text{ W}\cdot\text{m}^{-2}$).

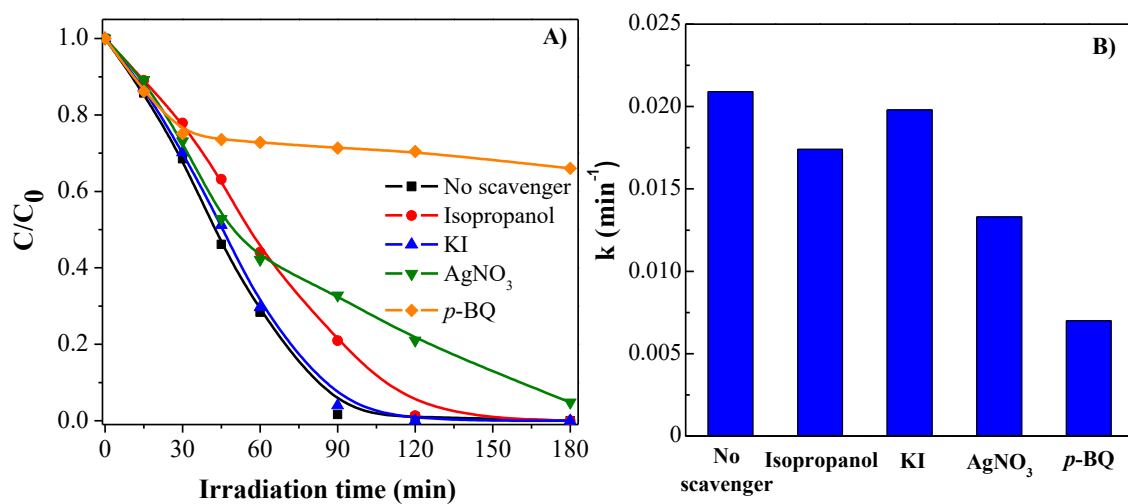


Figure 11. (A) ACE concentration profiles upon irradiation time and (B) values of the pseudo-first order rate constant of ACE disappearance (k) with TiZr15 photocatalyst using different scavengers at 1mM initial concentration. Operating conditions as in Figure 7.

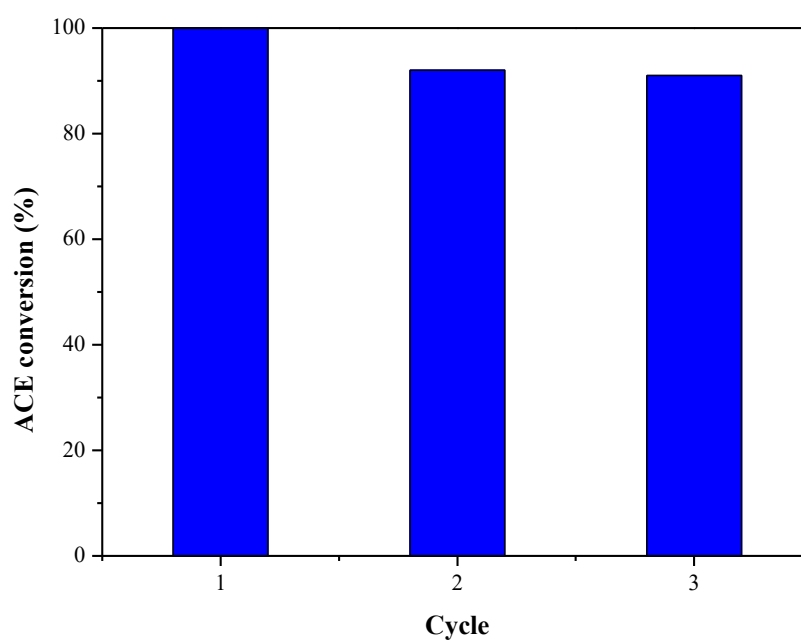


Figure 12. ACE conversion after 3 h of solar irradiation upon three successive runs with TiZr15. Operating conditions as Figure 7.

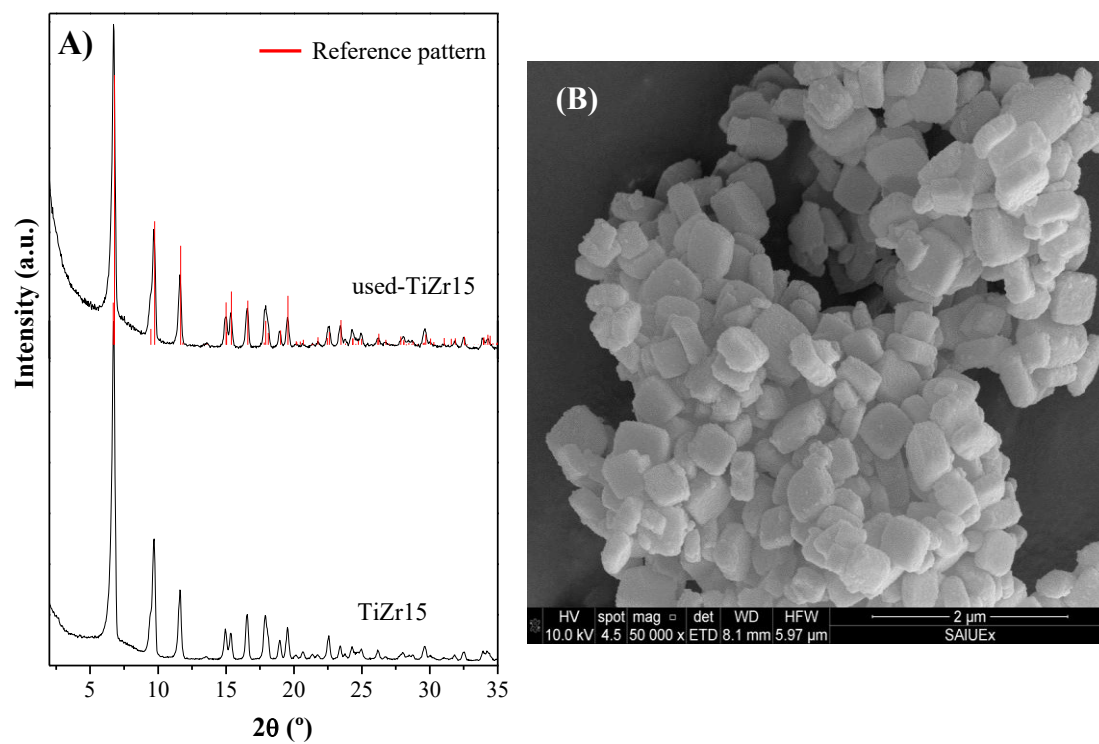
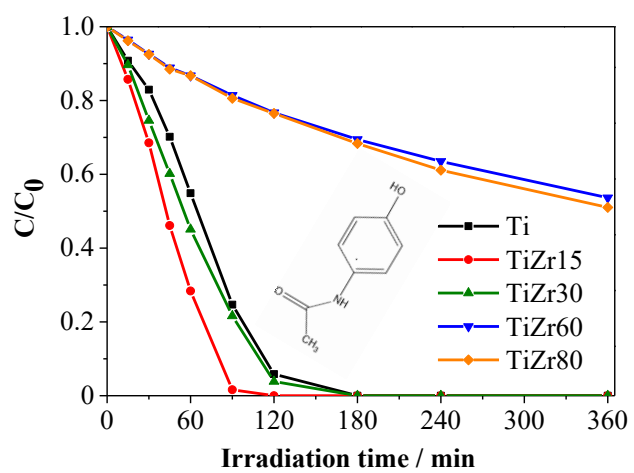
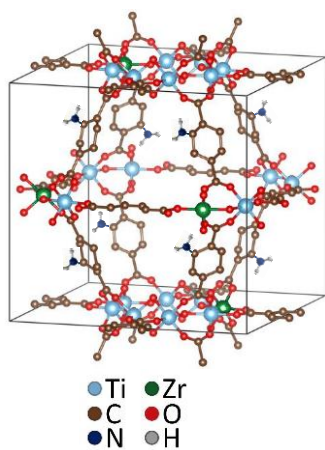


Figure 13. XRD pattern (A) and SEM image (B) of TiZr15 after the three successive runs.

GRAPHICAL ABSTRACT

NH₂-MIL-125 (Ti/Zr)



HIGHLIGHTS

- New mixed Ti-Zr MOFs were synthesized by the partial substitution of Ti by Zr.
- Higher activity for the acetaminophen solar photocatalytic degradation was obtained
- $\text{O}_2^{\bullet-}$ is the main contributing species in the photodegradation
- The new MOFs remain fairly stable after three successive runs

Supplementary Material

[Click here to download Supplementary Material: Electronic Supplementary Data.DOCX](#)

Mixed Ti-Zr metal-organic-frameworks for the photodegradation of acetaminophen under solar irradiation

A. Gómez-Avilés¹, M. Peñas-Garzón¹, J. Bedia^{1,*}, D.D. Dionysiou²,
J.J. Rodríguez¹, C. Belper¹

¹ *Departamento de Ingeniería Química, Universidad Autónoma de Madrid, Campus Cantoblanco, E-28049 Madrid, Spain*

² *Environmental Engineering and Science Program, Department of Chemical and Environmental Engineering (ChEE), 705 Engineering Research Center, University of Cincinnati, Cincinnati, OH 45221-0012, USA*

*Corresponding author. E-mail address: jorge.bedia@uam.es

Abstract

Mixed Ti-Zr metal-organic-frameworks (MOFs) have been synthesized and tested as photocatalysts under solar-simulated radiation using acetaminophen (ACE) as target pollutant. These materials were obtained upon partial substitution of Ti by Zr atoms in the crystalline structure of NH₂-MIL-125(Ti) MOF. The effect of the Ti:Zr molar ratio on their characteristics and catalytic behaviour has been analysed. Materials with high Zr relative amount (60-80%) showed amorphous structure and low solar-photocatalytic activity. In contrast, lower Zr proportions resulted in new MOFs with well-defined crystalline structure and high activity for the solar photocatalytic degradation of ACE, even higher than that of the bare Ti MOF. Results with scavengers allowed concluding that O₂^{•-} radicals are the main reactive species, although photogenerated [•]OH radicals and electrons also contribute to the degradation. The stability of the most active photocatalyst was confirmed upon three successive runs.

Keywords: Metal organic framework; NH₂-MIL-125; solar photocatalysis; water purification; acetaminophen.

1. Introduction

Metal-organic frameworks (MOFs) are hybrid materials composed of metal ions connected by organic linkers. These crystalline networks present structures with well-defined porosity, large specific surface area and the possibility of modulating their physicochemical properties by selecting different organic building blocks or metal clusters [1,3]. MOFs have attracted major attention in a wide range of applications, including gas storage [4,6], photoelectronic sensors [7,8], membrane processes [9,10] and environmental remediation [11]. Furthermore, these materials are gaining relevance as catalysts, including photocatalysts due to their semiconductor characteristics [12]. When a semiconductor solid is irradiated with an energy equal to or higher than its band gap, electrons (e^-) are promoted from the valence band (VB, formed by orbitals of the organic linker in the case of MOFs) to the conduction band (CB, associated to orbitals of the metal cluster in MOFs), generating holes (h^+) in the VB [1]. These photogenerated charges can be directed towards the surface of the material and be involved in the formation of powerful oxidizing species, which can degrade pollutant molecules. The earliest works dealing with MOFs used in photocatalytic water treatment date back to the beginning of the 2000's, when Yu et al. [13] proved the photocatalytic activity of these materials for the degradation of methylene blue dye. Later, Mahata et al. [14] explored the breakdown of selected organic dyes with three different coordination polymers. Since then, different modifications of MOFs, affecting both the organic linkers and/or the metal centres, have been researched to enhance their photocatalytic activity [15-17].

Regarding photocatalytic applications, many studies have used Ti-containing MOFs. One of the most widely analysed is $[Ti_8O_8(OH)_4(C_8H_6O_4)_6]$, denoted as MIL-125(Ti), which was synthesized for the first time by Dan-Hardi et al. [18] in 2009. MIL-125(Ti) presents a band gap energy of 3.6 eV (corresponding to a wavelength $\lambda = 345$ nm), being photoactive only under UV-light. Many efforts have been made to increase its photochemical activity towards the solar light, in order to avoid the use of UV-lamps and reduce the treatment cost. The incorporation of a $-NH_2$ group to the organic linker gives rise to NH_2 -MIL-125(Ti) MOF, $[Ti_8O_8(OH)_4(C_8H_5O_4NH_2)_6]$, allowing the donation of N_{2p} electrons of the aromatic structure to the amine group. This behaviour results in the formation of a redshifted band at the VB of the MOF, displacing the absorption band towards the visible region and reducing the band gap value (2.7 eV, $\lambda = 460$ nm) [19,20]. In addition to this, the amine group enhances the

charge transfer between metal and organic linker, the long-lived photoexcited states, inhibiting electron-hole recombination [1,2,21,22]. Zr-based MOFs have been also extensively studied in photocatalytic applications, being UiO-66 a well-known example of this kind of materials [23]. The presence of Zr^{4+} , a high oxidation state metal, gives rise to a strong coordination bonds with the organic linker [24,25]. Furthermore, it has been previously reported that Zr doping increases the solar photocatalytic activity of TiO_2 [26].

Emerging pollutants, including pharmaceuticals, personal care products, pesticides and hormones, are currently found in wastewaters and are considered potentially hazardous due to their harmful impact over the endocrine system and the environment [27,28]. Their removal from water streams is the focus of intense research and applications by the scientific community. The novelty of this study is the synthesis of new mixed Ti-Zr MOFs with different Ti:Zr molar ratios based on $\text{NH}_2\text{-MIL-125(Ti)}$. To the best of our knowledge, this is the first mixed Zr-Ti MOF apart from the previous reported by Lee et al. [29]. Although in that study, Ti was introduced in the Zr-based MOF in a postsynthetic exchange, while in our study we introduce Zr atoms in a Ti-based MOF in a single step, avoiding the use of postsynthetic steps. The solar photocatalytic activity of this material has been tested in the degradation of acetaminophen, as target emerging pollutant, in aqueous phase. This compound is a widely used antipyretic and analgesic pharmaceutical and its presence has been detected in urban wastewaters. Despite, $\text{NH}_2\text{-MIL-125(Ti)}$ has been recently used as photocatalyst for the reduction of heavy metals [30], the oxidation of alcohols and amines [31-33] and the degradation of dyes [19,20,34] under UV and visible light, to the best of our knowledge no previous works have reported on the synthesis of mixed Ti-Zr MOFs based on $\text{NH}_2\text{-MIL-125}$ and their application for the degradation of emerging pollutants.

2. Experimental

2.1. Materials synthesis

Pure $\text{NH}_2\text{-MIL-125(Ti)}$ was synthesized according to Martis et al. [35] with some modifications. 2-amino benzene dicarboxylic acid (6 mmol, Aldrich, 99%) was mixed with N,N-dimethylformamide (25 mL, DMF, Sigma-Aldrich, $\geq 99.8\%$) and stirred at room temperature for 5 min until total dissolution. Then, titanium isopropoxide (3 mmol, Aldrich, $\geq 97\%$) was added dropwise under continuous stirring until complete homogenization and afterwards methanol (25 mL, CH_3OH , Sigma-Aldrich, anhydrous 99.8%) was incorporated.

The mixture was stirred for 30 min, transferred to a 65 mL Teflon lined stainless steel autoclave, and heated for 16 h at 150 °C. After the solvothermal treatment, the resulting solid was separated by centrifugation (5000 rpm, 5 min). Further, it was washed twice with 100 mL of DMF for 30 min and twice with 100 mL of methanol during the same time, separating the resulting solid by centrifugation in all cases. The final yellow solid was dried at 60 °C overnight. This MOF was denoted as Ti. The mixed Ti-Zr MOFs were synthesized following the same procedure but with different Ti:Zr molar percentages combining zirconium (IV) butoxide solution (Aldrich, 80%wt in butanol) and titanium isopropoxide in the metal-precursor incorporation step of the synthesis. The mixed Ti-Zr MOFs were denoted according to the zirconium molar percentage incorporated, which was determined by wavelength-dispersive X-ray fluorescence (WDXRF). Four mixed-MOFs were prepared, denoted by TiZr15, TiZr30, TiZr60 and TiZr80.

2.2. Characterization

A Bruker D8 diffractometer with a Sol-X energy dispersive detector was used to record the X-ray diffraction (XRD) spectra from 2 to 50° of 2θ , using a Cu K α radiation and a recording rate equal to 1.5 °·min⁻¹. The (121) diffraction peak was used to calculate the average crystal size of the MOF and the UnitCell software [36] was used to estimate the cell parameters of the MOF unit crystal by a minimum square approximation. A TriStar 123 equipment (Micromeritics) was used to characterize the porous texture by N₂ adsorption-desorption at -196 °C. Prior to the analyses, the samples were outgassed under vacuum at 120 °C for 18 h. The BET method was used to calculate the specific surface area (S_{BET}). The micropore surface area (S_{MP}) and the external or non-microporous surface area (S_{EXT}) were obtained from the t-plot. The total pore volume (V_{T}) was assessed by the amount of nitrogen adsorbed (as liquid) at P/P_0 of 0.99. The density functional theory (DFT) was used to obtain the pore size distribution [37]. A Shimadzu 2501PC UV-vis spectrophotometer was employed for recording the UV-vis diffuse reflectance spectra (DRS) in the 250-800 nm range (BaSO₄ was chosen as reference). The spectra were used to obtain the band gap values of the photocatalysts, considering them as indirect semiconductors [38] (as TiO₂), using the Tauc Plot technique [39]. The amount of Ti and Zr in the different photocatalysts was determined by wavelength-dispersive X-ray fluorescence (WDXRF) using a Bruker S8 TIGER spectrometer under inert atmosphere (He) with a 4 kW Rh-anode X-ray tube (maximum voltage of 60 kV and maximum current of 170 mA). The composition was determined by

using Spectra Plus (v.3) software. Scanning electron microscopy (SEM) images were obtained with a Quanta 3D FEG apparatus from FEI COMPANY. A Bruker iFS 66VS spectrometer was used to record the Fourier Transform Infrared (FTIR) spectra, using a resolution of 2 cm^{-1} in the $4000\text{--}400\text{ cm}^{-1}$ wavenumber range. Raman spectra were obtained using a 532 nm laser μ Sense-LabC1X Enwave Optronics Raman Confocal equipment, coupled to an Olympus BX51 M microscope. Photoluminescence (PL) spectra of the materials were obtained via a Fluoromax-4 spectrofluorometer with an excitation wavelength of 420 nm.

2.3 Photocatalytic tests

The photocatalytic degradation of acetaminophen (ACE) (Sigma-Aldrich, >99%) was carried out in a Pyrex jacketed reactor (500 mL) at a controlled temperature of $20\text{ }^{\circ}\text{C}$ under magnetic stirring. This reactor was placed inside the chamber of a solar simulator (Suntest XLS+, ATLAS) with a Xe lamp and a “Daylight” filter (cuts off $\lambda \leq 290\text{ nm}$), capable of simulating solar radiation. The light intensity was set at $600\text{ W}\cdot\text{m}^{-2}$. In each test, a catalyst amount of $250\text{ mg}\cdot\text{L}^{-1}$ was dispersed in 150 mL aqueous solution containing an initial concentration of ACE of $5\text{ mg}\cdot\text{L}^{-1}$ at an initial pH equal to 6.9 (unless different conditions were indicated). The reactor was covered and the dispersion was maintained under stirring in dark for 1 h with the aim of achieving adsorption equilibrium. Afterwards, the solution was exposed to simulated solar light for 6 h. Samples of 0.45 mL were taken at different times, filtered with PTFE syringeless filters (Whatman $0.2\text{ }\mu\text{m}$) and analysed by HPLC (Shimadzu Prominence-I LC-2030C), using a diode array detector (SPD-M30A) and a C18 column (Eclipse Plus $5\text{ }\mu\text{m}$, Agilent). The chromatograms were registered using a gradient elution method where the mobile phase content (acetic acid aqueous solution 0.1%, Sigma Aldrich $\geq 99\%$) changes during elution with acetonitrile (Scharlau HPLC grade) at a rate of $0.56\%\cdot\text{min}^{-1}$, with a constant flow equal to $0.7\text{ mL}\cdot\text{min}^{-1}$. Blank tests were carried out without catalyst at the same conditions in order to check the stability of ACE under solar irradiation. Total organic carbon (TOC) was measured with a Shimadzu TOC equipment and organic acids from the ACE photodegradation were analysed by ionic chromatography with a Metrohm 883 Basic IC Plus equipment.

3. Results and discussion

3.1. Characterization

As indicated before, the incorporation of Zr^{4+} in the structure of $\text{NH}_2\text{-MIL-125(Ti)}$ MOF was accomplished by combining Ti^{4+} and Zr^{4+} alkoxide precursors in the desired ratio during the synthetic pathway. The chemical compositions of the samples, collected in Table S1 of the supplementary data, were determined by WDXRF analysis in order to quantify the final Ti/Zr molar ratios. These analyses confirm the successful incorporation of Zr^{4+} in the resulting material. Figure 1 represents the XRD spectra of the different Ti-Zr MOFs synthesized. The diffraction pattern of Ti sample (that without Zr) corresponds to that described in the literature for $\text{NH}_2\text{-MIL-125(Ti)}$ MOF [19,40,42]. In the case of the samples with Zr, those with lower amounts (TiZr15 and TiZr30) show diffraction patterns very similar to that of the Ti sample. In contrast, the diffractograms of the samples with higher amount of Zr (TiZr60 and TiZr80) do not show the characteristic peaks of the crystalline structure and only displayed a wide band at 2θ values close to 7° and associated to an amorphous structure. It seems that the incorporation of Zr in high proportion inhibits the crystallization of the MOF. It is also noteworthy that no other crystalline phases were found in the diffractograms.

Figure 1. XRD patterns. The characteristic peaks of the MIL-125 (ref. ja903726m_si_002.cif [18]) are included as reference (red colour).

The comparison between the diffraction patterns of Ti, TiZr15 and TiZr30 shows a slight negative shift of the most intense peak located at 6.79° of 2θ for Ti sample. This deviation could be attributed to some modification on the crystal lattice of the MOF due to the Zr incorporation. The crystal size and the lattice parameters were analysed in more detail (the data are collected in Table 1). The average crystal size (D) was established by the Scherrer's equation using the (121) peak ($2\theta = 11.6^\circ$). The most intense peak (011) centred at 6.79° was not used because the reference pattern revealed that it overlaps with a lower intensity peak (110) located at 6.69° [18]. The D values show that the incorporation of Zr caused a slight increase of the crystal size and it is interesting to note that TiZr15 and TiZr30 present similar D values, without the Zr percentage having a significant influence. The lattice parameters of the orthorhombic structure characteristics of $\text{NH}_2\text{-MIL-125}$ MOF are also modified by the Zr incorporation. This can be clearly observed in the values of a parameter and cell volume. The orthorhombic structure suffers a high expansion along the x direction accompanied by a certain increase of height (c parameter) and practically no variation in the y axis. These structural modifications are consequence of the substitution of Ti^{4+} in oxo-clusters by bigger

Zr⁴⁺ atoms [41,43], indicating that the synthetic route used in this work achieves the incorporation of Zr⁴⁺ into the NH₂-MIL-125 lattice without the formation of other crystalline phases, giving rise mixed Ti-Zr MOFs.

Table 1. Structural parameters.

Figure 2 shows characteristic SEM images of the synthesized materials. The morphology of Ti was thin and disk-like shapes with an average size of ca. 500 nm, in agreement with the morphology and size previously reported in the literature [34,44,45]. The introduction of Zr seems to have no relevant effect in the morphology of the resulting MOF up to Ti:Zr molar ratios of 70:30. In contrast, further increases in the amount of Zr provoked significant morphological changes. In the case of the TiZr60 sample disc-shaped particles were also obtained, although not so well-defined as those obtained with higher Ti:Zr ratios and with a significantly bigger size (around 1.0-1.5 μ m). Finally, the sample with the lowest Ti:Zr ratio (i.e. the highest Zr content, TiZr80) shows a completely amorphous structure. It seems that a high amount of Zr prevents the formation of crystalline structure. Probably other synthesis conditions, namely temperature or duration of the treatment, may lead to the formation of crystals.

Figure 2. SEM images of (A) Ti, (B) TiZr15, (C) TiZr30, (D) TiZr60 and (E) TiZr80.

Figure 3 depicts the N₂ adsorption–desorption isotherms at -196 °C of the synthesized samples. Ti exhibits a type I-like isotherm according to the IUPAC classification with no hysteresis loop, characteristic of a microporous structure and in agreement with previous works [40,46]. Increasing Zr proportion does not modify significantly the shape of the isotherms but clearly reduces the amount of N₂ adsorbed, thus indicating a significant decrease of the microporosity and the BET surface area. The effect is dramatically pronounced at the highest Zr proportions. It may be related to the amorphous character of these materials, without the characteristic channels structure of metal organic frameworks. It seems that the increase in the amount of Zr precursor in the synthesis stage hinders the crystallization, and the lack of a proper crystal lattice results in the loss of porosity. Table 2 summarizes the porous texture parameters of the materials synthesized. It can be seen the

dramatic decrease of BET surface area and micropore volume of the samples with higher Zr proportions. It is noteworthy that low Zr substitution yields a material (TiZr15) with high surface area, similar to that described by the non-Zr NH₂-MIL-125 MOF. The micropore size distributions obtained by DFT (Figure 4) show predominantly narrow microporous structures for the Ti-Zr MOFs with lower Zr proportions, which displace towards higher micropore widths as that proportion increases. These results indicate that while the Zr incorporation induces structural modifications, it does not develop a new porous network and pore tenability.

Figure 3. Nitrogen adsorption–desorption isotherms at -196 °C.

Table 2. Porous texture parameters and band gap values.

Figure 4. DFT pore size distributions.

Figure 5A depicts the UV-Vis absorption spectra of the samples. Ti shows two absorption bands at 280 and 370 nm. The first one is associated to the light absorption of Ti-oxo-clusters, while the second is due to the amine ligand-based absorption [30,41,42]. The introduction of Zr does not significantly affect these values of the absorption bands, except for lowest Ti:Zr molar ratios (TiZr60 and TiZr80). In these cases, the first absorption band shifted to lower wavelengths, ca. 260 nm, which can be attributed to the predominant absorption of Zr-oxo-clusters instead of Ti-oxo-clusters [41]. It is also noteworthy the slight shift in the visible range of absorption of TiZr60. The band gaps (E_g) of these materials were calculated from the Tauc plots (represented in Figure 5B) assuming that they are indirect semiconductors. The values are summarized in Table 2. The estimated band gap for Ti, 2.74 eV, is agreement with the values reported in previous works [19,20]. It corresponds to the electron transfer from the organic linker to the metal-oxo cluster, following the ligand-to-metal charge transfer mechanism [47]. The partial substitution of Ti⁴⁺ by Zr⁴⁺ in the crystal lattice reduces somewhat the band gap at low to moderate Zr content and then increasing the amount of Zr this effect disappears. Therefore, there is a given Ti:Zr ratio associated to a minimum band gap value, although of low significance. Figure S1 represents the light harvesting efficiency (LHE) values obtained from the UV-Vis absorption spectra. As can be seen, all the MOFs

show very similar values apart from TiZr60, which shows slightly higher LHE values in the visible light region.

Figure 5. (A) UV-Vis spectra and (B) Tauc plots.

Surface functional groups were analyzed by Fourier transform infrared (FTIR) spectra, as shown in Figure 6. For comparison purposes, the FTIR spectrum of the ligand used in the synthesis, 2-aminoterephthalic acid, was also included in the Figure. The peaks located at 3524 and 3410 cm^{-1} of the ligand can be assigned to the stretching of the $-\text{NH}_2$ groups [48]. In the case of the MOFs, these peaks probably are overlapped by the characteristic band of adsorbed water, situated around 3400 cm^{-1} , due to the $-\text{OH}$ stretching. Another peak related to the presence of adsorbed water was observed at 1620 cm^{-1} , assigned to the bending band of the $-\text{OH}$ group. The vibrations in the region between 1800 – 1100 cm^{-1} are related to the stretching of carboxylic, carbonyl and phenyl groups. In this sense, the stretching of the carboxylic acid group ($-\text{COOH}$, 1710 cm^{-1}) [49] presented higher intensity in the ligand precursor than in the MOFs, in which appeared in the form of a weak shoulder. This reduction in the $-\text{COOH}$ groups can be ascribed to the reaction with the metal cluster precursors, forming the structure of the MOF. Stretching of the $-\text{C}=\text{C}$ skeletal aromatic ring of the linker was observed in all synthesized samples at 1574 and 1335 cm^{-1} [50]. Vibration peaks at 1513 and 1435 cm^{-1} can be assigned to the stretching of the carbonyl asymmetric and symmetric groups from the linker, respectively [48]. In this region can also be observed the stretching of $-\text{C}-\text{N}$ (1255 cm^{-1} , characteristic of aromatic amines [50]) and the stretching vibration of $-\text{C}-\text{C}$ from the aromatic ring (1150 cm^{-1}). A last peak at 770 cm^{-1} can be associated to the out-of-plane $-\text{C}-\text{H}$ stretching [51]. The region below that peak is characterized by the vibration stretching bands (centered at 640 cm^{-1}) of $-\text{Ti}-\text{O}-\text{Ti}$ clusters and a peak at 450 cm^{-1} , corresponding to the bending vibration of these metal clusters [52]. The introduction of Zr^{4+} in the structure of the different TiZr MOFs did not show any new vibration peak but produced a reduction in the region ascribed to the vibration of the $-\text{Ti}-\text{O}-\text{Ti}$ clusters. That decrease in the intensity of the vibration was higher with increasing the molar proportion of zirconium, again confirming the successful substitution of Ti^{4+} by Zr^{4+} in the synthesis of these MOFs. Figure S2 shows the Raman spectra of the three different Ti/Zr-MOFs with successful crystalline structure. They present weak signals due to its fluorescence. The peaks at 1254 and 1422 cm^{-1} correspond to the bending and symmetric stretching of the $\text{Ti}-\text{O}-\text{Ti}-\text{O}$ framework.

This confirms that the -COOH group of the organic linker is directly connected to the Ti-oxo cluster [53]. The rest-identified peaks are associated to the organic linker. The peaks at 826 and 1126 cm^{-1} correspond to the C-H bending of the benzene ring and terephthalates rings breathing, respectively. The O=C=O symmetric stretching in carboxylate group of the organic linker appears at 1442 cm^{-1} . In contrast, the asymmetric stretching is present at 1580 cm^{-1} . On the other hand, the peak at 1278 cm^{-1} is related to the C=O stretching while 1626 cm^{-1} , to the C-C and N-H bond bending vibrations and C=C stretching of benzene ring [54,55]. In the case of TiZr15 and TiZr30 a new peak at 1592 cm^{-1} appears, probably due to the Zr incorporation.

Figure 6. FTIR spectra of Ti and TiZr MOFs (2-aminoterephthalic acid spectrum, used as ligand precursor in the synthesis of the MOFs, has also been included for comparison).

3.2. Photocatalytic tests

Before the photocatalytic tests, the adsorption capacity of the MOFs was quantified. In all cases, the adsorption equilibrium was reached in less than 1 h, describing almost negligible adsorption capacities, with ACE adsorbed amounts between 0.6 and 2% depending of the MOF. These extremely low values indicate the negligible effect of adsorption. Figure 7 represents the time-course of the ACE concentration upon solar irradiation with the synthesized Ti-Zr MOFs. In absence of photocatalyst, the ACE concentration remained constant after 6 h of irradiation, confirming the high stability of this compound under solar light. In the presence of the MOF photocatalysts two different behaviours were clearly observed. Those samples with the highest amounts of Zr (TiZr60 and TiZr80) yielded frankly poor ACE conversion, while at lower Zr proportion the incorporation of this metal improves the rate of ACE disappearance respect to the observed with the Ti MOF. These catalysts, TiZr15 and TiZr30, with a well-defined crystalline structure, allowed complete ACE degradation in less than 3 hours of irradiation in contrast with the non-crystalline materials with higher Zr content. The most promising sample, TiZr15, allowed complete ACE conversion after only 90 min of solar irradiation, probably as consequence of the optimum combination of a well-developed porosity and a lower band gap value resulting from the partial substitution of Ti^{4+} by Zr^{4+} in the structure of the MOF. Furthermore, the effect of charge recombination has also to be taken into account, as it will be shown below. The doping with Zr provides energy levels below the conduction band or above the valence band that can

act as new states for electron movements, improving the photocatalyst behaviour by decreasing the recombination of charges [56,57]. In order to verify this assumption, PL measurement were performed to investigate the recombination of photo-generated electron–hole pairs. In general, it is accepted that weak fluorescence intensity indicates a low charge recombination rate. Figure 8 represents the PL spectra of different photocatalysts. As can be seen, the incorporation of Zr into the MOF structure result in a significant decrease of the recombination, which can justify the higher photoactivity of these samples. In the case of the samples with the higher Zr content, TiZr60 and TiZr80, even lower recombinations are observed, probably due to the lower charge separation achieved with those amorphous samples.

Figure 7. Evolution of the ACE concentration under solar irradiation with the photocatalysts tested (20 °C; 250 mg·L⁻¹ of catalyst; initial acetaminophen concentration after the 1 h adsorption step \approx 5 mg·L⁻¹; intensity of irradiation: 600 W·m⁻²; pH=6.9; error bars: confidence intervals at 95%).

Figure 8. PL spectra.

We have not detected any aromatic intermediate by HPLC, probably due to their fast degradation to other organics and to the relatively low ACE initial concentration. We have also analyzed the effluent by ionic chromatography, and several short organic acids such as maleic, malonic and oxalic were detected. According to the literature [58], ACE photodegradation proceeds through the formation of hydroquinone, which undergoes oxidation to benzoquinone, which upon ring cleavage and further oxidation results in different carboxylic acids, including those detected in our study. We have also analyzed the TOC content of the water after the photocatalytic test (3 h of irradiation) when using the most active photocatalysts, TiZr15. The TOC reduction was 65.3%, indicating a significant mineralization degree. We have compared the photodegradation with TiZr15 and TiO₂ P25, which is considered the benchmark in the field (Figure S3). As can be seen in the photodegradation curves, the ZrTi15 photocatalyst shows a significant better photocatalytic

activity than that of TiO₂ P25 under solar irradiation. This result confirms the high activity ZrTi15 MOF-based photocatalyst synthesized in this study.

The rate of disappearance of ACE fitted well to a pseudo-first-order rate equation (the respective $\ln(C_0/C)$ vs. reaction time plots are shown in Figure S4 of supplementary data). The values of the apparent rate constant are given in Table 3. The highest value corresponds to TiZr15 sample, 1.7 times higher than that of the non-zirconium MOF (Ti). Since the incorporation of Zr does not lead to a considerable modification of the band gap or surface properties, this improvement in activity can be attributed to the presence of Zr ions that can act as charge trappers, leading to an increase of the charge carrier lifetimes and therefore avoiding the recombination processes and favouring the activity as supported by PL measurements (Figure 8). This effect has been also reported for other metal-doped semiconductors [26,59]. For the sake of comparison with other photocatalysts previously reported by our research group, tested under the same conditions, the photonic efficiency (ξ) has been determined following to the Serpone's method [60], considering the photon flux in these experiments equal to $6.38 \cdot 10^{-3}$ mol photon \cdot min⁻¹. The data for all synthesized MOFs are collected in Table 3. TiZr15 yielded a photonic efficiency of 1.89 einstein⁻¹, much higher than the obtained for the solar photocatalytic degradation of antipyrine with Zr-doped TiO₂ supported on delaminated clay photocatalysts (1.2 einstein⁻¹) [26], and those of TiO₂-ZnO/clay materials for the degradation of acetaminophen under solar light whose maximum value reached 1.0 einstein⁻¹ [61]. Even, the Ti and TiZr30 samples were more efficient than previous reported catalysts. Thus, these new mixed Ti-Zr metal organic frameworks appear promising photocatalysts for the removal of water pollutants using solar light as energy source. Table 4 summarizes the highest photocatalytic degradation rate of acetaminophen obtained in this study with other previously reported, all of them obtained under solar irradiation. The highest rate constant, 0.0121 min⁻¹, is much higher than that previously reported by our research group for the solar photocatalytic degradation of antipyrine with Zr-doped TiO₂ supported on delaminated clay photocatalysts (0.0098 min⁻¹) [26]. We also reported on the photodegradation of acetaminophen under solar light with ZnO/sepiolite [62] and Ag/ZnO-TiO₂/clay heterostructures [63]. The maximum values of the pseudo first-order rate constant were 0.0032 and 0.0095 min⁻¹, respectively, also bellow than the obtained with the best photocatalysts described in the current work. Jallouli et al. [64] reported a slight

lower rate constant using TiO₂/cellulosic fibers photocatalysts. However, higher rate constants were reported when using Pt/TiO₂ [58] and C-modified TiO₂ [65] photocatalysts.

Table 3. Values of the pseudo-first order rate constant of ACE disappearance under solar irradiation with the catalysts tested.

Table 4. Comparison of pseudo-first order rate constants of ACE disappearance.

Regarding the optimal parameters of reaction with TiZr15, different tests were carried out to analyze the effects of the initial photocatalyst dosage and the initial pH on the ACE photodegradation. The evolution of the acetaminophen concentrations at different photocatalyst loadings are depicted in Figure 9. The best results in terms of photocatalytic activity were obtained with a 250 mg·L⁻¹ TiZr dosage. The increase of the photocatalyst dosage beyond this point results in the decrease of the photodegradation of ACE, probably as a consequence of the poorer penetration of light within the solution. Another important parameter of the reaction is the initial pH of the solution. The results obtained for different initial pH in the range 3 to 11 using TiZr15 as photocatalyst can be observed in Figure 10. In acidic medium (pH ≤ 5), the performance of the TiZr15 was remarkably reduced. This can be ascribed to the scavenging effect over the O₂^{•-} (the main specie involved in the oxidation of the ACE, as shown below in Figure 11) by protons, resulting in the formation of the hydroperoxide radical (HO₂[•], with a lower oxidant power compared to O₂^{•-} [66]). A lower conversion of ACE was also obtained in strong basic medium (pH = 11), due to the degradation of the catalyst. In this sense, the characteristic yellow-colored TiZr15 sample was turned into a lighter color when the reaction was carried out at an initial pH of 11. From these results, it can be concluded that a catalyst dose of 250 mg·L⁻¹ and neutral or slight basic initial pH are the more suitable conditions for the best performance of the TiZr15 MOF.

Figure 9. Evolution of ACE concentration under solar light at different initial TiZr15 dosages (20 °C; initial ACE concentration ≈ 5 mg·L⁻¹; intensity of irradiation: 600 W·m⁻²; pH=6.9).

Figure 10. Evolution of ACE concentration under solar light with TiZr15 at different initial pH (20 °C; 250 mg·L⁻¹ of catalyst; initial acetaminophen concentration after adsorption \approx 5 mg·L⁻¹; intensity of irradiation: 600 W·m⁻²).

To learn on the reactive species involved in the photodegradation process, tests with different scavengers (IPA, p-BQ, KI or AgNO₃) were carried out, using the most active photocatalyst TiZr15. Isopropanol (IPA) was used to trap the hydroxyl radicals (\cdot OH) [67], benzoquinone (p-BQ) for the superoxide radicals ($O_2^{\cdot-}$) [68], potassium iodide (KI) as electron (e^-) acceptor, while silver nitrate (AgNO₃) was used for holes (h^+) [69,70]. In all cases, the scavenger was used at 1 mM concentration, without modifying any other reaction condition. Figure 11A shows the evolution of ACE concentration upon irradiation time in presence of different scavengers at 1 mM starting concentration. The values of the pseudo-first order rate constants of ACE disappearance are also included (Figure 11B). It can be observed that the addition of KI, a hole scavenger, had no significant effect, being the results almost similar to the obtained in the absence of this scavenger. This suggests a negligible participation of holes in the photodegradation of ACE. In contrast, the rate of photocatalytic decomposition of ACE decreased in different extents with the addition of IPA, AgNO₃ and p-BQ, \cdot OH, electron and $O_2^{\cdot-}$ scavengers, respectively. The last showed the most pronounced effect, suggesting that $O_2^{\cdot-}$ is the main contributing radical in the photocatalytic process investigated with the TiZr MOF tested. It is important to remark that the behaviour of the different oxidizing species might vary depending on the pollutant-photocatalyst system and the solution pH. For example, the degradation of rhodamine B dye has been reported to be primarily due to $O_2^{\cdot-}$ and h^+ with both Bi₂MoO₆/UiO-66(Zr) [71] and BiOBr/NH₂-MIL-125(Ti) [19] photocatalysts. In contrast, $O_2^{\cdot-}$ and \cdot OH were the main contributing species in the photodegradation of this dye with Ag/MIL-125 as photocatalyst [17]. \cdot OH radicals are considered the dominant oxidizing species in a wide range of photocatalytic reactions, including the oxidation of pharmaceuticals [61,63]. Nevertheless, our results point to $O_2^{\cdot-}$ as the main responsible in this case (pH₀=6.9). These species can be generated by the interaction of photogenerated electrons with O₂ adsorbed at the MOF surface.

Figure 11. (A) ACE concentration profiles upon irradiation time and (B) values of the pseudo-first order rate constant of ACE disappearance (k) with TiZr15 photocatalyst using different scavengers at 1 mM initial concentration. Operating conditions as in Figure 7.

The stability and reusability of the photocatalyst is a crucial issue regarding potential applications. The stability of the best photocatalyst was checked upon three successive runs. In each cycle, the dispersion was maintained under stirring in dark for 1 h and then was exposed to solar light irradiation for 3 h. Then, the photocatalyst was separated by filtration and simply washed with distilled water and dried at 60 °C prior use in the following run. The reaction conditions were the same as those described before. Figure 12 represents the ACE conversion achieved after 3 h of solar irradiation in the three successive runs with TiZr15. The photocatalytic activity decreased slightly after the first cycle and then remained almost unchanged from the second to the third runs, in which conversion values above 90% were maintained. After the third use the catalyst was characterized by XRD and SEM (Figure 13). Additionally, N₂ adsorption-desorption isotherm (Figure S5) and WDXRF (Table S1) were also carried out. The diffraction pattern remained almost unchanged with no apparent displacement of the characteristic diffraction peaks and without additional ones. No significant morphological changes were observed from the SEM images of the used catalyst (Figure 13B) respect to the first one (Figure 2B). There are no notable changes in the N₂ isotherm shape (Figure S5) nor in the chemical composition (Table S1), just the surface area suffered a slight decrease, from 1036 to 930 m²·g⁻¹, probably due to the presence of adsorbed molecules that blockage part of the porous network. Thus, TiZr15 appears as a promising photocatalyst for degradation of emerging contaminants with a high stability.

Figure 12. ACE conversion after 3 h of solar irradiation upon three successive runs with TiZr15. Operating conditions as Figure 7.

Figure 13. XRD pattern (A) and SEM image (B) of TiZr15 after the three successive runs.

4. Conclusions

Mixed Ti-Zr MOFs based on NH₂-MIL-125 were successfully synthesized with different Ti:Zr molar ratios within a wide range. At low to moderate Zr proportions these materials show the same crystalline structure that NH₂-MIL-125, although with a higher average crystal size and an expanded unit cell, due to the substitution of Ti⁴⁺ by Zr⁴⁺. They show high surface area values and essentially microporous texture. Nevertheless, at higher Zr amounts materials with amorphous structure and much lower porosity were obtained. The crystalline TiZr15

yielded the highest activity for the solar photocatalytic degradation of acetaminophen, even higher than that of the non-zirconium MOF, allowing complete ACE conversion after 90 min, well below the reaction time required with other catalysts tested by our group in previous works [26,61,63]. PL measurements indicate that the incorporation of Zr into the MOF structure results in a significant decrease of the recombination, which can justify the higher photoactivity of these samples. Experiments with scavengers lead to the conclusion that $O_2^{\cdot-}$ is the main contributing species in the photodegradation of ACE, although photogenerated $\cdot OH$ radicals and electrons are also partly involved. TiZr15 remains fairly stable after three successive runs, maintaining its crystalline structure and morphology unchanged and allowing more than 90% ACE conversion under the operating conditions tested.

Acknowledgements

The authors acknowledge the financial support from Spanish MINECO (project CTQ2016-78576-R). M. Peñas-Garzón thanks Spanish MECD for FPU16/00576 grant. Authors thank the Research Support Services of the University of Extremadura (SAIUEx) for its technical and scientific support. We also thank to Dr. Juan Cabanillas for his help with PL measurements.

References

- [1] J. Qiu, X. Zhang, Y. Feng, X. Zhang, H. Wang, J. Yao, Modified metal-organic frameworks as photocatalysts, *Appl. Catal. B: Environ.* 231 (2018) 317-342.
- [2] M.B. Chambers, X. Wang, L. Ellezam, O. Ersen, M. Fontecave, C. Sanchez, L. Rozes, C. Mellot-Draznieks, Maximizing the photocatalytic activity of metal-organic frameworks with aminated-functionalized linkers: Substoichiometric effects in MIL-125-NH₂, *J. Am. Chem. Soc.* 139 (2017) 8222–8228.
- [3] H. Furukawa, N. Ko, Y.B. Go, N. Aratani, S.B. Choi, E. Choi, A.Ö. Yazaydin, R.Q. Snurr, M. O’Keeffe, J. Kim, O.M. Yaghi, Ultrahigh porosity in metal-organic frameworks. *Sci.* 329 (2010) 424-428.
- [4] B. Szczeńniak, J. Choma, M. Jaroniec, Gas adsorption properties of hybrid graphene-MOF materials, *J. Colloid Interface Sci.* 514 (2018) 801-813.

- [5] Q.-G. Zhai, N. Bai, S. Li, X. Bu, P. Feng, Design of Pore Size and Functionality in Pillar-Layered Zn-Triazolate-Dicarboxylate Frameworks and Their High CO₂/CH₄ and C₂ Hydrocarbons/CH₄ Selectivity. *Inorg. Chem.* 54 (2015) 9862-9868.
- [6] A.R. Millward, O.M. Yaghi, Metal-organic frameworks with exceptionally high capacity for storage of carbon dioxide at room temperature, *J. Am. Chem. Soc.* 127 (2005) 17998-17999.
- [7] G.-Y. Zhang, C. Cai, S. Cosnier, H.-B. Zheng, X.-J. Zhang, D. Shan, Zirconium-metalloporphyrin frameworks as a three-in-one platform possessing oxygen nanocage, electron media, and bonding site for electrochemiluminescence protein kinase activity assay, *Nanoscale* 8 (2016) 11649-11657.
- [8] V. Stavila, A.A. Talin, M.D. Allendorf, MOF-based electronic and opto-electronic devices, *Chem. Soc. Rev.* 43 (2014) 5994-6010.
- [9] W. Li, Y. Zhang, Q. Li, G. Zhang, Metal-organic framework composite membranes: Synthesis and separation applications. *Chem. Eng. Sci.* 135 (2017) 232-257.
- [10] S. Qiu, M. Xue, G. Zhu, Metal-organic framework membranes: from synthesis to separation application, *Chem. Soc. Rev.* 43 (2014) 6116-6140.
- [11] N.A. Khan, Z. Hasan, S.H. Jhung, Adsorptive removal of hazardous materials using metal-organic frameworks (MOFs): A review. *J. Hazard. Mater.* 244-245 (2013) 444-456.
- [12] C.-C. Wang, J.-R. Li, X.-L. Lv, Y.-Q. Zhang, G. Guo, Photocatalytic organic pollutants degradation in metal-organic frameworks. *Energ. Environ. Sci.* 7 (2014) 2831-2867.
- [13] Z.-T. Yu, Z.-L. Liao, Y.-S. Jiang, G.-H. Li, G.-D. Li, J.-S. Chen, Construction of a microporous inorganic-organic hybrid compound with uranyl units, *Chem. Comm.* 10 (2004) 1814-1815.
- [14] P. Mahata, G. Madras, S. Natarajan, Novel photocatalysts for the decomposition of organic dyes based on metal-organic framework compounds, *J. Phys. Chem. B* 110 (2006) 13759-13768.
- [15] L. Chen, R. Luque, Y. Li, Controllable design of tunable nanostructures inside metal-organic frameworks. *Chem. Soc. Rev.* 46 (2017) 4614-4630.
- [16] C. Yang, X. You, J. Cheng, H. Zheng, Y. Chen, A novel visible-light-driven In-based MOF/graphene oxide composite photocatalyst with enhanced photocatalytic activity toward the degradation of amoxicillin, *Appl. Catal. B Environ.* 200 (2017) 673-680.

- [17] H. Guo, D. Guo, Z. Zheng, W. Weng, J. Chen, Visible-light photocatalytic activity of Ag@MIL125(Ti) microspheres, *Appl. Organometal. Chem.* 29 (2015) 618–623.
- [18] M. Dan-Hardi, C. Serre, T. Frot, L. Rozes, G. Maurin, C. Sanchez, G. Férey, A new photoactive crystalline highly porous titanium(IV) dicarboxylate, *J. Am. Chem. Soc.* 131 (2009) 10857-10859.
- [19] S.-R. Zhu, P.-F. Liu, M.-K. Wu, W.-N. Zhao, G.-C. Li, K. Tao, F.-Y. Yi, L. Han, Enhanced photocatalytic performance of BiOBr/NH₂-MIL-125(Ti) composite for dye degradation under visible light, *Dalton Trans.* 45 (2016) 17521-17529.
- [20] R.M. Abdelhameed, A.M.S. Silva, J. Rocha, Enhanced photocatalytic activity of MIL-125 by post-synthetic modification with Cr(III) and Ag nanoparticles. *Chem. A Eur. J.* 21 (2015) 11072-11081.
- [21] J. G. Santaclara, M. A. Nasalevich, S. Castellanos, W.H. Evers, F.C.M. Spoor, K. Rock, L.D.A. Siebbeles, F. Kapteijn, F. Grozema, A. Houtepen, J. Gascon, J. Hunger, M.A. van der Veen, Organic Linker Defines the Excited- State Decay of Photocatalytic MIL- 125(Ti)- Type Materials, *Chem. Sus. Chem.* 9 (2016) 388-395.
- [22] M. de Miguel, F. Ragon, T. Devic, C. Serre, P. Horcajada, H. García, Evidence of photoinduced charge separation in the metal-organic framework MIL-125(Ti)-NH₂, *Chem. Phys. Chem.* 13 (2012) 3651-3658.
- [23] J.H. Cavka, S. Jakobsen, U. Olsbye, N. Guillou, C. Lamberti, S. Bordiga, K.P. Lillerud, A new zirconium inorganic building brick forming metal organic frameworks with exceptional stability, *J. Am. Chem. Soc.* 130 (2008) 13850-13851.
- [24] B. Wang, X.-L., Lv, D. Feng, L.-H. Xie, J. Zhang, M. Li, Y. Xie, J.-R. Li, H.-C. Zhou, Highly stable Zr(IV)-based metal-organic frameworks for the detection and removal of antibiotics and organic explosives in water, *J. Am. Chem. Soc.* 138 (2016) 6204-6216.
- [25] G. Férey, C. Mellot-Draznieks, C. Serre, F. Millange, J. Dutour, S. Surble, I. Margiolaki, A chromium terephthalate-based solid with unusually large pore volumes and surface area. *Sci.* 309 (2005) 2040-2042.
- [26] C. Belver, J. Bedia, J.J. Rodriguez, Zr-doped TiO₂ supported on delaminated clay materials for solar photocatalytic treatment of emerging pollutants, *J. Hazard. Mat.* 322 (2017) 233–242.

- [27] J. Rivera-Utrilla, M. Sánchez-Polo, M.A. Ferro-García, G. Prados-Joya, R. Ocampo-Pérez, Pharmaceuticals as emerging contaminants and their removal from water. A review. *Chemosphere* 93 (2013) 1268–1287.
- [28] P. Amrita, K. Yew-Hoong Gin, A. Yu-Chen Lin, M. Reinhard, Impacts of emerging contaminants on freshwater resources: review of recent occurrences, sources, fate and effects, *Sci. Total Environ.* 408 (2010) 6062–6069.
- [29] Y. Lee, S. Kim, J. Kang, S.M. Cohen, Photocatalytic CO₂ reduction by a mixed metal (Zr/Ti), mixed ligand metal–organic framework under visible light irradiation, *Chem. Commun.* 51 (2015) 5735–5738.
- [30] H. Wang, X. Yuan, Y. Wu, G. Zeng, X. Chen, L. Leng, Z. Wu, L. Jiang, H. Li, Facile synthesis of amino-functionalized titanium metal-organic frameworks and their superior visible-light photocatalytic activity for Cr(VI) reduction, *J. Hazard. Mater.* 286 (2015) 187–194.
- [31] Z. Wu, X. Huang, H. Zheng, O. Wabg, G. Hai, W. Dong, G. Wang, Aromatic heterocycle-grafted NH₂-MIL-125(Ti) via conjugated linker with enhanced photocatalytic activity for selective oxidation of alcohols under visible light. *Appl. Catal. B Environ.* 224 (2018) 479–487.
- [32] Y. Fu, L. Sun, H. Yang, L. Xu, F. Zhang, W. Zhu, Visible-light-induced aerobic photocatalytic oxidation of aromatic alcohols to aldehydes over Ni-doped NH₂-MIL-125(Ti), *Appl. Catal. B Environ.* 187 (2016) 212–217.
- [33] D. Sun, L. Ye, Z. Li, Visible-light-assisted aerobic photocatalytic oxidation of amines to imines over NH₂-MIL-125(Ti), *Appl. Catal. B Environ.* 164 (2015) 428–432.
- [34] S. Hu, M. Liu, K. Li, C. Song, G. Zhang, X. Guo, Surfactant-assisted synthesis of hierarchical NH₂-MIL-125 for the removal of organic dyes, *RSC Adv.* 7 (2017) 581–587.
- [35] M. Martis, W. Meicheng, K. Mori, H. Yamashita, Fabrication of metal nanoparticles in metal organic framework NH₂-MIL-125 by UV photo-assisted methods for optimized catalytic properties, *Catal. Today* 235 (2014) 98–102.
- [36] T.J.B. Holland, S.A.T. Redfern, Unit cell refinement from powder diffraction data: the use of regression diagnostics, *Miner. Mag.* 61 (1997) 6577.
- [37] J. Landers, G.Y. Gor, A.V. Neimark, Density functional theory methods for characterization of porous materials, *Colloids Surf. A: Physicochem. Eng. Asp.* 437 (2013) 3–32.

- [38] J. Zhang, P. Zhou, J. Liu, J. Yu, New understanding of the difference of photocatalytic activity among anatase, rutile and brookite TiO₂, *Phys. Chem. Chem. Phys.* 16 (2014) 20382–20386.
- [39] J. Tauc, Absorption edge and internal electric fields in amorphous semiconductors, *Mater. Res. Bull.* 5 (1970) 721–726.
- [40] S.N. Kim, J. Kim, H.Y. Kim, H.Y. Cho, W.S. Ahn, Adsorption/catalytic properties of MIL-125 and NH₂-MIL-125, *Catal. Today* 204 (2013) 85–93.
- [41] D. Sun, W. Liu, M. Qiu, Y. Zhang, Z. Li, Introduction of a mediator for enhancing photocatalytic performance via post-synthetic metal exchange in metal-organic frameworks (MOFs), *Chem. Comm.* 51 (2015) 2056-2059.
- [42] C.H. Hendon, D. Tiana, M. Fontecave, C. Sanchez, L. D'Arras, C. Sassoey, L. Rozes, C. Mellot-Draznieks, A. Walsh, Engineering the optical response of the titanium-MIL-125 metal-organic framework through ligand functionalization. *J. Am. Chem. Soc.* 135 (2013) 10942-10945.
- [43] Y.-F. Li, D. Xu, J.I. Oh, W. Shen, X. Li, Y. Yu, Mechanistic study of codoped titania with nonmetal and metal ions: A case of C-Mo Codoped TiO₂, *ACS Catal.* 2 (2012) 391-398.
- [44] Y.-H. Fan, S.-W. Zhang, S.-B. Qin, X.-S. Lia, S.-H. Qia, An enhanced adsorption of organic dyes onto NH₂ functionalization titanium-based metal-organic frameworks and the mechanism investigation, *Microp. Mesop. Mater.* 263 (2018) 120-127.
- [45] M. Oveisi, M. Alina Asli, N. Mohammad Mahmoodi, MIL-Ti metal-organic frameworks (MOFs) nanomaterials as superior adsorbents: Synthesis and ultrasound-aided dye adsorption from multicomponent wastewater systems, *J. Hazard. Mater.* 347 (2018) 123–140.
- [46] C. Zlotea, D. Phanon, M. Mazaj, D. Heurtaux, V. Guillermin, C. Serre, P. Horcajada, T. Devic, E. Magnier, F. Cuevas, G. Férey, P.L. Llewellyn, M. Latroche, Effect of NH₂ and CF₃ functionalization on the hydrogen sorption properties of MOFs, *Dalton Trans.* 40 (2011) 4879–4881.
- [47] J. Bedia, V. Muelas-Ramos, M. Peñas-Garzón, A. Gómez-Avilés, J.J. Rodríguez, C. Belver. A review on the synthesis and characterization of metal organic frameworks for photocatalytic water purification, *Catalysts*, 9 (2019) 52–95.
- [48] S. Hu, M. Liu, K. Li, Y. Zuo, A. Zhang, C. Song, G. Zhang, X. Guo, X, Solvothermal synthesis of NH₂-MIL-125(Ti) from circular plate to octahedron, *Cryst. Eng. Comm.* 16 (2014) 9645–9650.

- [49] D. Mohan, K.P. Singh, S. Sinha, D. Gosh, Removal of pyridine from aqueous solution using low cost activated carbons derived from agricultural waste materials, *Carbon* 42 (2004) 2409–2421.
- [50] M. Oveisi, M.A. Asli, N.M. Mahmoodi, MIL-Ti metal-organic frameworks (MOFs) nanomaterials as superior adsorbents: Synthesis and ultrasound-aided dye adsorption from multicomponent wastewater systems, *J. Hazard. Mater.* 347 (2018) 123–140.
- [51] J. Bedia, R. Barrionuevo, J. Rodríguez-Mirasol, T. Cordero, Ethanol dehydration to ethylene on acid carbon catalysts, *Appl. Catal. B Environ.* 103 (2011) 302–310.
- [52] M. Shafaei, E.K. Goharshadi, M. Mashreghi, M. Sadeghinia, TiO₂ nanoparticles and TiO₂@graphene quantum dots nanocomposites as effective visible/solar light photocatalysts, *J. Photochem. Photobiol. A Chem.* 357 (2018) 90–102.
- [53] P. Karthik, R. Vinoth, P. Zhang, W. Choi, E. Balaraman, B. Neppolian, π – π interaction between metal–organic framework and reduced graphene oxide for visible-light photocatalytic H₂ production, *ACS Appl. Energy Mater.* 1 (2018) 1913–1923.
- [54] I. Strauss, A. Mundstock, D. Hinrichs, R. Himstedt, A. Knebel, C. Reinhardt, D. Dorfs, J. Caro, The interaction of guest molecules with Co-MOF-74: A Vis/NIR and Raman approach, *Angew. Chemie - Int. Ed.* 57 (2018) 7434–7439.
- [55] C. Atzori, G.C. Shearer, L. Maschio, B. Civalleri, F. Bonino, C. Lamberti, S. Svelle, K.P. Lillerud, S. Bordiga, Effect of benzoic acid as a modulator in the structure of UiO-66: An experimental and computational study, *J. Phys. Chem. C* 121 (2017) 9312–9324.
- [56] F. Fresno, M.D. Hernández-Alonso, D. Tudela, J.M. Coronado, J. Soria, Photocatalytic degradation of toluene over doped and coupled (Ti,M)O₂ (M = Sn or Zr) nanocrystalline oxides: Influence of the heteroatom distribution on deactivation, *Appl. Catal. B: Environ.* 84 (2008) 598–606.
- [57] J. Lukác, M. Klementová, P. Bezdieka, S. Bakardjieva, J. Subrt, L. Szatmáry, Z. Bast, J. Jirkovsky, Influence of Zr as TiO₂ doping ion on photocatalytic degradation of 4-chlorophenol, *Appl. Catal. B* 74 (2007) 83–91.
- [58] O. Nasr, O. Mohamed, A.-S. Al-Shirbini, A.-M. Abdel-Wahab, Photocatalytic degradation of acetaminophen over Ag, Au and Pt loaded TiO₂ using solar light, *J. Photochem. Photobiol. A: Chem.* 374 (2019) 185–193.
- [59] P. Bouras, E. Stathatos, P. Lianos, Pure versus metal-ion-doped nanocrystalline titania for photocatalysis, *Appl. Catal. B: Environ.* 73 (2007) 51–59.

- [60] N. Serpone, Relative photonic efficiencies and quantum yields in heterogeneous photocatalysis, *J. Photochem. Photobiol. A* 104 (1997) 1-12.
- [61] M. Tobajas, C. Belver, J.J. Rodriguez, Degradation of emerging pollutants in water under solar irradiation using novel TiO₂-ZnO/clay nanoarchitectures, *Chem. Eng. J.* 309 (2017) 596–606.
- [62] M. Akkari, P. Aranda, C. Belver, J. Bedia, A. Ben Haj Amara, E. Ruiz-Hitzky, ZnO/sepiolite heterostructured materials for solar photocatalytic degradation of pharmaceuticals in wastewater, *Appl. Clay Sci.* 156 (2018) 104-109.
- [63] C. Belver, M. Hinojosa, J. Bedia, M. Tobajas, M.A. Alvarez, V. Rodríguez-González, J.J. Rodriguez, Ag-coated heterostructures of ZnO-TiO₂/delaminated montmorillonite as solar photocatalysts, *Materials* 10 (2017) 960-977.
- [64] N. Jallouli, K. Elghniji, H. Trabelsi, M. Ksibi, Photocatalytic degradation of paracetamol on TiO₂ nanoparticles and TiO₂/cellulosic fiber under UV and sunlight irradiation, *Arabian Journal of Chemistry* 10 (2017) S3640-S3645.
- [65] A. Gómez-Avilés, M. Peñas-Garzón, J. Bedia, J.J. Rodriguez, C. Belver, C-modified TiO₂ using lignin as carbon precursor for the solar photocatalytic degradation of acetaminophen, *Chem. Eng. J.* 358 (2019) 1574-1582.
- [66] E. Brillas, I. Sirés, M.A. Oturan, Electro-fenton process and related electrochemical technologies based on fenton's reaction chemistry, *Chem. Rev.* 109 (2009) 6570–6631.
- [67] L. Ye, J.Y. Liu, Z. Jiang, T.Y. Peng, L. Zan, Facets coupling of BiOBr-g-C₃N₄ composite photocatalyst for enhanced visible-light-driven photocatalytic activity, *Appl. Catal. B Environ.* 142 (2013) 1–7.
- [68] M.C. Yin, Z.S. Li, J.H. Kou, Z.G. Zou, Mechanism investigation of visible light-induced degradation in a heterogeneous TiO₂/Eosin Y/Rhodamine B system, *Environ. Sci. Technol.* 43 (2009) 8361–8366.
- [69] G. Li, K.H. Wong, X. Zhang, C. Hu, J.C. Yu, R.C.Y. Chan, P.K. Wong, Degradation of Acid Orange 7 using magnetic AgBr under visible light: The roles of oxidizing species. *Chemosphere* 76 (2009) 1185-1191.
- [70] Q.B. Li, X. Zhao, J. Yang, C.J. Jia, Z. Jin, W.L. Fan, Exploring the effects of nanocrystal facet orientations in g-C₃N₄/BiOCl heterostructures on photocatalytic performance, *Nanoscale* 7 (2015) 18971–18983.

[71] J. Ding, Z. Yang, C. He, X. Tong, Y. Li, X. Niu, H. Zhang, UiO-66(Zr) coupled with Bi_2MoO_6 as photocatalyst for visible-light promoted dye degradation, J. Colloid Interface Sci. 497 (2017) 126-133.